Preliminary studies for the development of Neural Network for fission trigger in the FRØZEN project

Brigitte Pertille Ritter
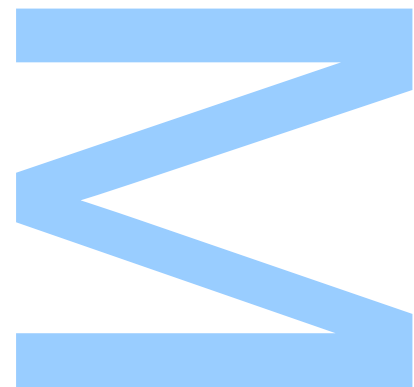
Master in Engineering Physics
Physics and Astronomy Department
2023

Supervisor
João Manuel Viana Parente Lopes, Auxiliar Professor
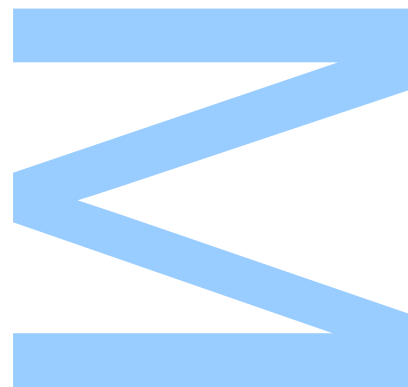University of Porto

Cosupervisor
Matthieu Lebois, Lecturer and Researcher
CNRS - DELEGATION IDF GIF-SUR-YVETTE
Université Paris-Saclay

Acknowledgements

Resumo

No âmbito do projeto "Fission Reaction at Orsay with Zero Emission of Neutrons" (FRØZEN), nas instalações do ALTO, no IJCLab em Orsay, foi realizada uma experiência de 5 semanas denominada "N-SI-125" com o intuito de estudar as correlações entre as diferentes emissões de partículas no processo de desexcitação de fragmentos de fissão. O espectrômetro de raios gama ν-Ball2 foi complementado com uma Câmara de Ionização de Grade-Frisch Dupla (IC) que desempenha diversas funções. Ela serve de referência para reconhecimento de eventos de fissão e é usada como referência temporal para a medida do tempo de voo que serve para a discriminação entre diferentes partículas emitidas na reação. Ela permite a medição das propriedades cinemáticas dos fragmentos de fissão (FF), como energia cinética e ângulo de emissão, *etc*. Existem algumas propriedades dos sinais gerados pela câmara que justificam a aquisição de dados como traços, visando uma melhor resolução temporal e cálculos, como o tempo de deriva de elétrons.

A primeira parte deste trabalho consiste na análise dos traços dos 9 canais de saída da câmara de ionização com métodos usuais, uma técnica extensa e demorada. Muitos parâmetros para cada canal da IC devem ser ajustados para melhorar as resoluções temporal e de energia. O sinal obtido pelo cátodo da câmara é particularmente relevante para optimizar as capacidades de determinação temporal. Os 4 planos de fio e os 4 canais de ânodo fornecem informações importantes sobre a deposição de energia no detector. Uma vez que os melhores parâmetros são encontrados e todos os dados podem ser analisados, o tempo de computação ainda é uma grande desvantagem. Embora o cálculo de energia tenha sido dominado com sucesso, a reconstrução do instante que ocorre a fissão nuclear se mostrou muito mais desafiadora. Os espectros, coincidência temporal, figuras de reconstrução de tempo de deriva e ângulo e estatísticas de tempo de computação são apresentados.

A segunda parte deste trabalho concentra-se no desenvolvimento de redes neurais totalmente conectadas para prever os resultados da análise baseada exclusivamente nos traços brutos. A previsão dos valores de energia foi muito bem-sucedida mas, devido a restrições de tempo, a avaliação da resolução temporal não pôde ser finalizada para avaliação das previsões das redes neurais. As figuras obtidas pela reconstrução do instante de fissão nuclear indicam uma boa previsão. Por outro lado, o tempo de deriva não pôde ser bem previsto com os modelos de rede neural projetados. Devido a limitações de tempo, outras abordagens, como redes neurais recursivas ou convolucionais, não puderam ser testadas.

Apesar dos desafios deste trabalho exploratório, resultados promissores foram encontrados, pois o consumo de tempo das redes neurais para prever as características dos traços da IC é consideravelmente menor do que a outra técnica usada.

Palavras-chave: análise de traços, análise de traços de uma câmara de ionização, rede neural para análise de traços, rede neural totalmente conectada

Abstract

In the scope of the Fission Reaction at Orsay with Zero Emission of Neutron (FRØZEN) project, a 5-week experiment labelled "N-SI-125" was held at the ALTO facility in IJCLab at Orsay to investigate the correlations between individual fission fragment pairs and fission observables to describe the entire fission fragment de-excitation process. The ν-Ball2 gamma spectrometer was complemented with a double Frisch-Grid Ionisation Chamber (IC) that serves a few purposes. It is the fission tag of the experiment, recognising fission events. It is used as a time reference to measure the time-of-flight used to discriminate different particles emitted in the reaction. It allows the determination of the fission fragments (FF) kinematic properties, such as kinetic energy and the emission angle. There are some properties of chamber output signals that justify the data acquisition as sampler or traces; hence, the trace analysis aims for better time resolution and calculations such as the electron drift-time.

The first part of this work consists of performing the trace analysis of the 9 signal outputs of the ionisation chamber with usual methods, an extensive and time-consuming technique. Many parameters for each chamber channel must be tuned to improve time and energy resolutions. While the cathode is more relevant for optimising the time determination capabilities, the 4 wire planes and 4 anode channels give important information on the deposited energy. Once the best parameters are found, and all data can be analysed, the computing time is still a major drawback. While the energy calculation was successfully mastered, the trigger time presented to be much more challenging. The spectra, time coincidence, drift time and angle reconstruction figures, and computing time statistics are presented.

The second part of this work focuses on developing Fully Connected Neural Networks to predict the results of our initial analysis solemnly based on the raw traces. The energy values prediction was very successful, and due to time constraints, the evaluation of time resolution could not be finalised. The figures for trigger time distribution seemed to be well predicted. The drift time, on the other hand, could not be well predicted with the neural network models designed. Due to time constraints, other approaches, such as recursive or convolutional neural networks, couldn't be tested.

Despite the challenges of this exploratory work, promising results were found as the time consumption of the neural networks prediction of the IC trace features is considerably smaller than the initial technique.

Keywords: trace analysis, ionisation chamber trace analysis, neural network for trace analysis, fully-connected neural network

Résumé

Dans le cadre du projet "Fission Reaction at Orsay with Zero Emission of Neutrons" (FRØZEN), une expérience de 5 semaines intitulée "N-SI-125" a été menée à l'installation ALTO de l'IJCLab à Orsay afin d'étudier les corrélations entre les différentes emissions de particules dans le processus de désexcitation des fragments de fission. Le spectromètre γ appelé ν-Ball2 a été complété par une double chambre d'ionisation à grille Frisch (IC) qui remplit plusieurs fonctions. Elle sert de référence pour la reconnaissance des évènements de fission et est utilisée comme référence temporelle pour la mesure de temps de vol qui servira à la discrimination des différentes particules émise dans la réaction. Elle permet aussi la mesure des propriétés cinématiques des fragments de fission (FF), telles que : l'énergie cinétique, l'angle d'émission, *etc.* Certaines propriétés des signaux générés par la chambre justifient l'acquisition de données sous forme d'échantillons ou de traces; par conséquent, l'analyse de ces dernières vise à obtenir une meilleure résolution temporelle et à effectuer des calculs tels que le temps de dérive des électrons.

La première partie de ce travail consiste en l'analyse des traces des 9 voies de signaux de la chambre d'ionisation avec des méthodes habituelles, une technique exhaustive et chronophage. De nombreux paramètres pour chaque canal de la chambre doivent être réglés pour améliorer la résolution temporelle et énergétique. Un soin particulier concernant une des voies: "la cathode" sera apporté afin d'optimiser les capacités de détermination des temps. Les 4 plans de fils et les 4 canaux d'anodes fournissent des informations importantes sur les dépôts d'énergie dans le détecteur. Une fois les meilleurs paramètres trouvés et toutes les données analysées, le temps de calcul reste un inconvénient majeur. Alors que le calcul de l'énergie a été maîtrisé avec succès, le temps de déclenchement s'est révélé beaucoup plus difficile. Les spectres, les coïncidences temporelles, les figures de temps de dérive et de reconstruction d'angle, ainsi que les statistiques sur le temps de calcul sont présentés.

La deuxième partie de ce travail se concentre sur le développement de réseaux neuronaux entièrement connectés pour prédire les résultats de l'analyse basée uniquement sur les traces brutes. La prédiction des valeurs d'énergie a été très réussie, et en raison de contraintes de temps, l'évaluation de la résolution temporelle n'a pas pu être finalisée. Les figures de distribution du temps de déclenchement semblaient bien prédites. En revanche, le temps de dérive n'a pas pu être bien prédit avec les modèles de réseaux neuronaux conçus. En raison de contraintes de temps, d'autres approches, telles que les réseaux neuronaux récursifs ou convolutionnels, n'ont pas pu être testées.

Malgré les défis de ce travail exploratoire, des résultats prometteurs ont été obtenus, car la consommation de temps des réseaux neuronaux pour la prédiction des caractéristiques des traces de la IC est considérablement plus faible que celle de la première technique.

Mots-clés : analyse des traces, analyse des traces de chambre d'ionisation, réseau neuronal pour l'analyse des traces, réseau neuronal entièrement connecté

Contents

List of Tables

List of Figures

Introduction

Nuclear fission is a complex process that is still not completely understood even after 85 years of study since its discovery. Energy partition and angular momentum generation mechanism are still puzzles that challenge the most advanced theoretical approaches [32]. For example, a better comprehension of the angular momentum distribution of the primary fission fragments (FF) provides information on the fissioning nucleus from the saddle point until shortly after scission. The FF de-excitation process involves the successive emission of prompt γ-rays and prompt neutrons, relevant parameters for nuclear applications.

To partly characterise fission mechanism properties, different researches have been conducted to measure the γ rays emitted from fission of several actinide[1].The advancement of scintillator detectors with both better time and energy resolution allows better precision on statistical features of the prompt fission gamma rays.

Motivation

The Fission Reaction at Orsay with Zero Emission of Neutron (FRØZEN) project intends to investigate the correlations between individual fission fragment pairs and fission observables to describe the entire fission fragment de-excitation process [3]. The interest in the study of fission events with no neutron emission is the γ-ray being responsible for evacuating all the excitation energy and the angular momentum. From these (rare) events, it will be possible to understand the minimal amount of excitation energy from which γ emission starts (above or below the neutron separation threshold). Such a deexcitation process is also a good probe to understand the nuclear structure above the particle emission threshold.

Therefore, a setup capable of performing γ spectrometry of prompt fission γ-rays, counting with high efficiency the number of emitted neutrons and correlating these measurements with a fission event is required.

To measure the γ energy simultaneously to the neutron count, the experimental setup

---

[1]Actinide: any of the series of fifteen metallic elements from actinium (atomic number 89) to lawrencium (atomic number 103) in the periodic table. They are all radioactive, the heavier members being extremely unstable and not of natural occurrence.

must combine high efficiency fast γ detectors with an efficient neutron counter and a detector to detect fission fragments, which serves as a clear fission trigger.

The response function of the detectors can be extremely complicated with fissioning systems with high activity, increasing the difficulty of processing and analysing the data by conventional analysis methods. Therefore, there is an interest in the future development of a neural network (NN) that could identify when fission occurred (that defines a so-called "trigger") based on the response function of the detectors, which is very useful for complex systems. If such a method is proven to be effective, then the use of a dedicated detector could become unnecessary. So far, similar trigger techniques have already been implemented in high-energy physics but not in nuclear physics. Applying machine learning techniques, we can further study the correlation between meaningful parameters in a fission reaction. The preliminary studies for that NN starts with the characterisation of the data obtained from an ionisation chamber that allows reconstructing the kinematics of the fission fragments and is also the fission trigger in our setup.

The work here presented consists of the analysis of the ionisation chamber traces obtained in a 5-week experiment held at the ALTO facility in Orsay, France, in March-April 2023. During my 6-months stay at Orsay as an intern at the Laboratoire de physique des deux infinis Irène Joliot-Curie, I began my work by performing the trace analysis of the ionisation chamber from February to mid-March with a very small amount of data[2] obtained from a previous campaign held at the end of October 2022. With the start of the new campaign approaching, I first had to focus on assembling the setup and finding solutions to the challenges and technical issues faced, as is extensively discussed further in this work. During the experiment, I performed a very quick analysis to cross-check the validity and quality of the data we were acquiring. After the end of the campaign, I started a much more careful and precise trace analysis, following known methods to obtain relevant information from each trace, such as energy deposited, fission fragment angle of emission and time.

It was followed by exploratory work on developing neural networks that are trained with the results obtained in the previous step. The NN output is expected to provide similar results, with a better or worse resolution, and it is of interest to comprehend to which extent NN can be used for trace analysis.

Details on the experiment, analysis methods and their performances are discussed in the following sections.

---

[2]Many challenges were faced during that campaign resulting in only 10 minutes of data acquisition with half of the chamber working.

Chapter 1

Theoretical background

This chapter is divided into two main topics, which are crucial for contextualising this work: A brief introduction to nuclear fission and an introduction to artificial neural networks and their application in experimental nuclear physics experiments.

1.1 Brief introduction to nuclear fission

Nuclear fission is a reaction mechanism consisting of a nucleus splitting into two individual nuclei with the same neutron-to-proton ratio as the fissioning system. Heavy atomic nuclei remain stable due to the balance between the Coulomb repulsion, the nuclear surface tension, and the quantum shell effects. Low kinetic energy nuclei fission occurs when that balance breaks spontaneously or when it is triggered by a projectile such as thermal neutrons in reactor cores.

In the context of induced fission, the absorbed energy causes deformation and, therefore, nucleus instability that might lead it to a "saddle point" configuration if there is enough energy to pass over its activation energy barrier to the fission reaction. The instant the fission occurs is the "scission point", and the nascent fission fragments (FF) rapidly move apart due to Coulomb repulsion. A schematic view of the significant steps in the fission reaction is represented in Figure 1.1. The time scale of each step is represented on the X-axis of this figure. The saddle point corresponds to the second step in the red region, while the scission corresponds to the separation line between the red and yellow areas.

Just after scission, the fission fragments are left with a large amount of excitation energy (~ 20 MeV) and angular momentum ($\sim 15 - 20\overline{h}$). This enormous amount of energy is released from the neutron-rich "primary fragments" by mass loss with neutron evaporation and γ deexcitation. Emitting the excess neutrons would be the most efficient way of minimising the system's energy. Hence, the γ emission would start when there is insufficient energy in the system – close to the neutron emission threshold. When the neutron emission stops and the deexcitation occurs through γ emission, the FF are called "secondary fragments" or "fission product".
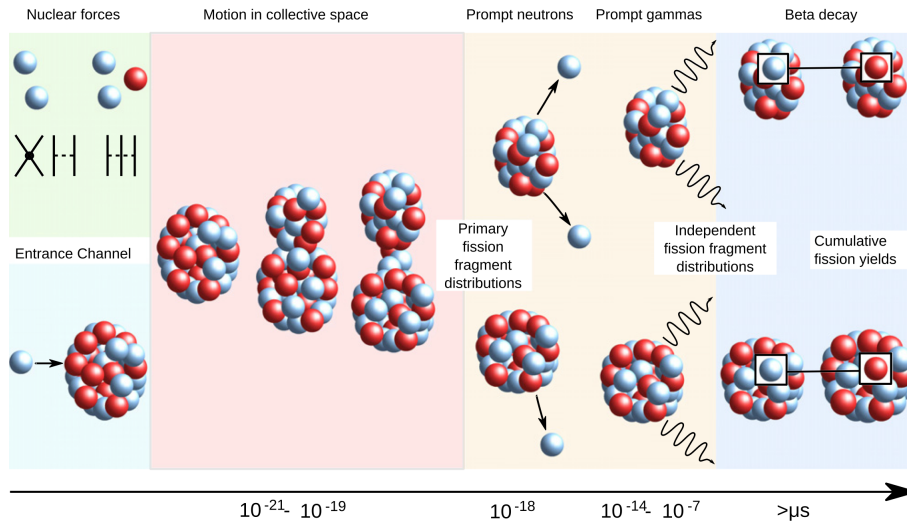
Figure 1.1: Schematic representation of the different stages of a fission process. Taken from [11].

A diagram representing the total excitation energy *versus* the total angular momentum of a fission fragment is found in Fig. 1.2. It is known that fission fragments enter this diagram at high energy and high spin (represented by the red oval). By first emitting neutrons, the FF fragment releases its energy to reach the pink oval close to the neutron emission threshold. Then, the remaining excitation energy and angular momentum can be released through γ emission.
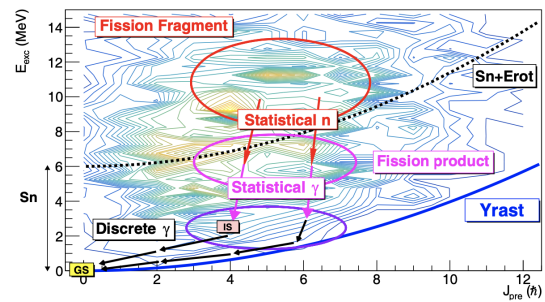
Figure 1.2: Fission fragments de-excitation process. Taken from [1].

However, experimentally, it has been observed that the total prompt γ energy is significantly higher than if the γ emission started after the excess neutrons evaporated.[2] These results bring forward a crucial question about the competition between neutron and γ emission to de-excite FF, which is the core motivation of the FRØZEN (Fission Reaction at Orsay with Zero Emission of Neutrons) project.

For more details, L. Qi, in his Ph.D. thesis, indicates that competition between neutron and γ emission starts sooner than initially expected. His experimental work was based on the spectrometry of so-called "Prompt Fission γ-rays". L. Qi demonstrated that more energy is emitted under the form of γ than expected if the γ emission started only at the neutron separation threshold.

1.1.1 Radioactive sources

From the possible mechanisms to study the neutron-gamma competition, the FRØZEN project chose a ^{252}Cf spontaneous fission source.

With a fission rate of ~3000 Bq, in 5 weeks of data acquisition, we could reach the minimum amount of data to have enough statistics to conduct a proper analysis. To have enough statistics using LICORNE neutron beam, for example, it would require 1500 years of LICORNE beam time (Fig. 1.3) [2].
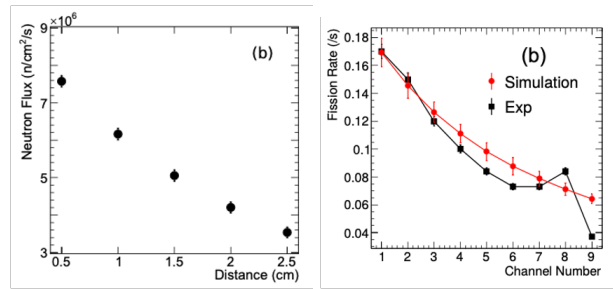
Figure 1.3: Neutron flux *versus* distance from the target (left) and fission rate (right). Taken from [2].

The spontaneous fissioning system used in the experiment, which will be referenced throughout this work, is ^{252}Cf, which is placed inside the ionisation chamber detector. We take this opportunity to also introduce the γ calibration sources used in this work for testing detectors: ^{60}Co and ^{137}Cs. The cobalt and cesium were used to determine the time resolution. Other sources were also used for calibrating the detectors, but this part of the analysis is not discussed in this work.

^{252}Cf **decay**

The radioisotope ^{252}Cf decays mostly by alpha emission, corresponding to 96.91%, and by spontaneous fission with a probability of 3.09% [20]. It has a half-life of 2645 years and is an intense neutron emitter, greatly used in nuclear reactors.

^{60}Co **decay**

One of the many uses of ^{60}Co is calibrating radiation-detection equipment due to its relatively long half-life of 5.27 years, high activity and energetic gamma emissions.

A simplified decay scheme is found in Fig. 1.4. It decays through beta emission to a ^{60}Ni* excited state, which will decay to the ground state by emitting energetic gammas of 1.1732 MeV and 1.3325 MeV.[21]
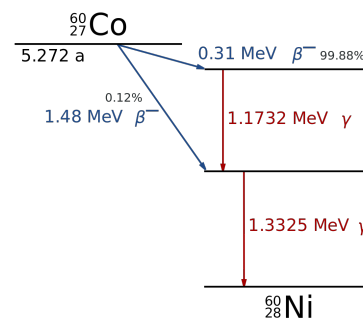
Figure 1.4: ^{60}Co decay scheme. Taken from [15]

The physical properties of cobalt bring some advantages in safety due to its bulk oxidation resistance and low solubility in water.

Cesium, on the other hand, is highly soluble in water, increasing the contamination risks. For this very reason, only sealed sources can be manipulated at ALTO. The deexcitation cascade of two γ consists of an excellent reference to test the timing properties of a γ spectrometry setup. From an energy point of view, it is used as a reference to evaluate the energy resolution of some of the detectors of the ν-Ball2 setup.

^{137}Cs **decay**

Similarly to ^{60}Co, ^{137}Cs is used to calibrate radiation-detection equipment due to its relatively long half-life of 30.05 years, high activity and energetic gamma emissions. As Fig. 1.5 illustrates, the decay scheme of ^{137}Cs, with 94.6% decays by beta emission to a metastable nuclear isomer[1] of barium ^{137m}Ba and 5.4% that decays directly to barium ground state ^{137}Ba.
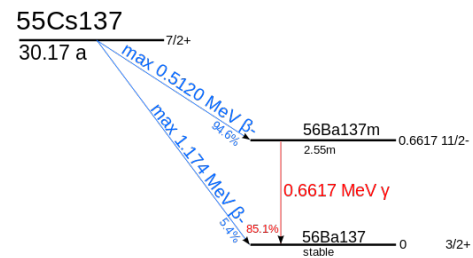
Figure 1.5: ^{137}Cs decay scheme. Taken from [14]

While ^{137}Cs half-life is three decades, ^{137m}Ba has a half-life of 153 seconds and decays to barium ground state emitting gamma rays of 661.2 keV [22]. This mono-energetic γ source is considered as a reference for energy resolution of scintillation detectors used in the ν-Ball2 setup.

1.2   State-of-the-art analysis techniques in Nuclear Physics based in Artificial Intelligence

A nuclear physics experiment produces thousands of data files with millions of events to be analysed. The preliminary analysis alone requires evaluating several variables, data calibration and time alignment of several detector channels, which is a time-consuming and computationally expensive procedure. Some research groups have started training neural networks designed for their specific setup to recognise patterns and classify data more efficiently than usual techniques.

Artificial neural networks (NN) are already used for neutron/γ discrimination in the neutron detectors of NEDA (NEutron Detector Array)[17]. In the scope of their project, there was a higher difficulty in performing the Pulse Shape Discrimination techniques between neutrons and γ-rays at low energies, which became possible with the use of NN. While they state the general performances were similar, the computing time is significantly better, and one of the NNs implemented was also more robust when processing misaligned waveforms. Still, on neutron/γ discrimination, another research group successfully developed an NN with an unsupervised learning algorithm, which also proved to be helpful to optimise traditional analysis techniques parameters[16].

Neural Networks for Pulse Shape Discrimination (PSD) also proved itself useful for the identification of pile-up pulses produced in organic scintillators [19]. Two types of NN were implemented, a Fully Connected NN and a Recurrent NN, and both have outperformed the traditional approach by reducing the misclassification of neutrons, gammas and pile-up pulses by 3, 14 and 11 times, respectively. Their NN proved to be capable of recovering

---

[1]Metastable nuclear isomers are higher excited states of nuclei which could undergo a gamma decay, but are comparatively long-lived typically due to high spin stabilisation.[9]

and identifying neutron and gamma-ray compositions from the pile-up pulses in high pulse rate scenarios.

Neural networks have proven to be useful and potentially faster and more efficient than the usual techniques known today, raising the question of the limits and application of AI in the data analysis of nuclear fission experiments. For a better comprehension of this work, an introduction to artificial neural networks and their vocabulary is presented in the following.

1.2.1 Artificial Neural Networks

Different artificial intelligence (AI) types have been implemented to predict results based on previous training data sets. One of the forms of AI implementation is artificial neural networks inspired by human brain neural networks.
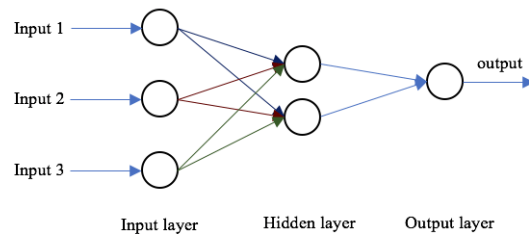
Figure 1.6: Simple neural network architecture. Taken from [30]

A simple example of an NN structure consists of an input layer with n_i neurons or n_i inputs, one or more hidden layers with n_h neurons and an output layer with one or more neurons, depending on the number of outputs.

1.2.2 Neural network architecture and parameters

Depending on the input data used for training and the expected relation between it, different NN can be implemented.

A NN model can be built for complex and multiple input and output data. The input layer of a NN is designed to receive the data in the desired format and return the output layer. In between, there are one or more hidden layers, which will perform correlations between the adjacent layers, converging to a result that minimises the loss. The number of neurons in the hidden layers is usually between the number of neurons in the input and output layers. After training, the NN can be applied to unknown data sets to either find the target value or label.

Parameters

The following equation gives the output of a single neuron:

$$Y = \sum_i (weight_i \cdot input_i) + bias \tag{1.1}$$

- **Weights** define how much the output depends on the input. The higher the weight, the more dependent it is.

- **Biases** are an additional input into the next layer that will always have an initial value of 1, being independent of the previous layer. This guarantees that even when all the inputs are zeros, there will still be activation in the neuron.

Hyperarameters

The hyperparameters of a neural network determine its architecture and learning approach.

- **Activation functions** decide if a neuron should be activated, and weights and biases should be calculated, introducing a non-linearity between input and output layers. Some of the most common activation functions are the Sigmoid function, Softmax function, Hyperbolic Tangent function (Tanh) and Rectified Linear Unit (ReLU) function. While Sigmoid is mostly used for binary classification and Softmax for multi-class classification, Tanh is suitable for predicting values between -1 and 1 and ReLU between 0 and 1.
- **Batch size** is the number of data used in each iteration[2]. It directly affects the training speed and convergence. The smaller the batch size, the longer it takes to converge. The batch size is usually a power of two for better computing performance.
- **Dropout rate** is a parameter set for randomly dropping a fraction of the neurons during training, avoiding overfitting the data. It is a regularisation[3] technique.
- **Epochs** is the number of times the neural network training processes the entire training data set.
- **Learning rate** is how fast or slow the weights and biases are updated and converge to a solution. A model that learns too fast will most probably skip the optimal solution. At the same time, an extremely slow learning rate might find a solution that doesn't comprehend the overall behaviour of the data because it might consider data situations with lower statistics as outliers.
- **Number of hidden layers** and the number of neurons in each layer are part of the architecture and greatly impact the final output prediction. The more complex the data, the more hidden layers are required. In a Physics context, where most relations are first or second order, one or two hidden layers are usually enough.
- **Optimiser** algorithm adjusts the parameters of a NN; it reduces overall loss and improves accuracy.

---

[2]The total number of iterations is given by the number of epochs times the data set size divided by the batch size.

[3]Regularisation technique in machine learning and deep learning is used to prevent overfitting and improve the generalisation performance of a model by adding a penalty term to the loss function during training.[26]

Supervised vs. unsupervised learning

There are two different learning approaches a neural network can follow: supervised and unsupervised learning.

Supervised learning learns from a data set with labels or target values to predict the output based on the input features. It can be used for both classification and regression. In classification, the NN assign data points to predefined classes (labels). In regression, it predicts a continuous numerical value (target value).

On the other hand, unsupervised learning learns from data without any information on the expected outcome, exploring the data's inherent structures and correlations. It is commonly used for clustering[4], dimensionality reduction[5] and anomaly detection (outliers).

1.2.3 Neural Networks and trace analysis

The first important step in developing an NN is to comprehend the input data and have an intuition on the type of relation expected to be found. In a Physics context, the relations are usually linear or of second order, so we expect to have a neural network of one or two hidden layers. There are many situations where NNs are used and require a much higher amount of hidden layers to be able to predict behaviours. Details on the NN structure and hyperparameters are presented in Chapter 4.

---

[4]Clustering algorithm groups a set of objects in such a way that objects in the same group (cluster) are, in a way, more similar to each other than to those in other groups (clusters)

[5]Dimensionality reduction refers to techniques that reduce the number of input variables in a data set, preserving the most relevant information[12].

Chapter 2

Experimental Setup of the N-SI-125 experiment

From March 20th to April 24th 2023, an experiment labelled "N-SI-125" dedicated to the study of fission fragment de-excitation process was performed at the ALTO facility of IJ-CLab. A γ spectrometer named "ν-Ball2" was installed for a full experimental campaign. Five weeks of this campaign were dedicated to the FRØZEN experiment. For that occasion, an ionisation chamber was coupled ν-Ball2 setup to fully characterise the de-excitation of nascent fission fragments, which emits a cascade of prompt γ and prompt neutrons and the FF kinetic energy. In the following, details about the measurement setup, the different detectors and data acquisition will be presented.

2.1 Experimental setup

2.1.1 ν-Ball2 setup

The ALTO facility has a long tradition of hosting γ spectroscopy campaigns. Over the past ten years, several spectrometers were built, and each time, their performances increased [7]. Hosted by the ALTO facility, the ν-Ball2 is the last generation of a spectrometer. It combines germanium and PARIS detectors (LaBr$_3$:NaI phoswichs) and uses the FASTER data acquisition system. In other words, ν-Ball2 can perform detailed fine spectroscopy and fast timing with sub-nanosecond precision as well as its predecessor ν-Ball [28].

Germanium detectors

The backbone of the spectrometer is made of 24 Compton-suppressed high-purity germanium clovers (HPGe) placed in two rings around 90° (75.5° and 104.5°) with respect to the fissioning source. They are represented as greys trapezoidal boxes on the right panel in figure 2.1. The typical energy resolution expected for these detectors is about 2.7 keV at 1.33 MeV. Their time resolution is about $10 - 15$ ns. In the context of the FRØZEN ex-
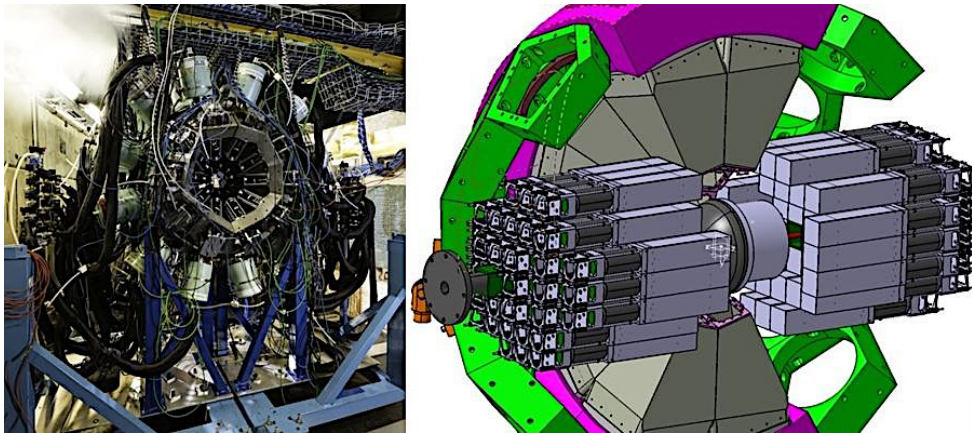
Figure 2.1: ν-Ball2 setup: the ionisation chamber is placed in the centre of the spherical structure that holds the Ge detectors (photo on the left), and the PARIS phoswichs complete a spherical geometry around the chamber. Taken from [28]

periment, these detectors will be used to identify fission fragments due to some specific γ energies emitted in their de-excitation. On a daily basis, these detectors need to be cooled down to cryogenic temperatures. More information about that specificity is given in HPGe clovers cooling system section 2.1.4.

PARIS array

The ν-Ball2 spectrometer is also made of 72 PARIS[4] phoswich that combines LaBr$_3$(Ce) and NaI crystals. The purpose of these detectors is to provide a good time selection to separate γ rays and neutrons and also to provide a good detection efficiency at energies higher than 2 MeV. One drawback of these detectors is their intrinsic activity of a LaBr$_3$(Ce) detector that is presented in Fig. 2.2. The LaBr$_3$ has a good energy resolution for a scintillator de-

Figure 2.2: LaBr$_3$(Ce) detector intrinsic activity. Taken from [10]

tector (3% at 662 keV and 0.6% at 18 MeV) and an efficiency higher than 60% for detected gammas up to 10 MeV. Also, typical time resolution for phoswiches is announced to be below 1 ns [4]. Ideally, it would be interesting to have a very long LaBr$_3$ crystal, but that would be challenging and costly, so the solution is to combine cubic LaBr$_3$ (2"x2"x2") with NaI (2"x2"x6") crystal with an optical coupling. The NaI crystal is used for high-energy photons and neutrons measurement because they need more crystal depth to lose energy in the crystal material until the interaction occurs. Despite PARIS not being designed for neutron detection, it is possible to measure them with the cost of lower efficiency.

2.1.2   Ancillary detectors

After describing the main features of the spectrometer, one must understand that this setup can be tweaked to adapt to specific experimental needs. This adaptation is performed by adding additional detectors named "ancillary detectors". For this experiment, and as it has been explained previously, one ancillary detector consists of an ionisation chamber. The other will be a small $LaBr_3$ crystal that will serve as a reference for time reconstruction of physical events during the data analysis procedure.

THALIA

THALIA is a $LaBr_3$ detector placed in ν-Ball2 structure, used to determine the time-of-flight and perform the time alignment between the ionisation chamber and the remaining detectors. To achieve the best time precision, the signals were acquired as electronic signal frames (later referred to as traces). The analysis method used is later described in subsection 3.1.5.

Ionisation chamber

A position-sensitive double Frisch-Grid Ionisation Chamber (dFGIC) was used in this experiment. This type of IC allows the determination of the fission fragments (FF) kinematic properties, such as energy and the emission angle.

A scheme of the interior of the IC is presented in the right panel of figure 2.3. It shows the various part of the chamber that allows the detection of the fission fragment propagation in the gas contained in the chamber.
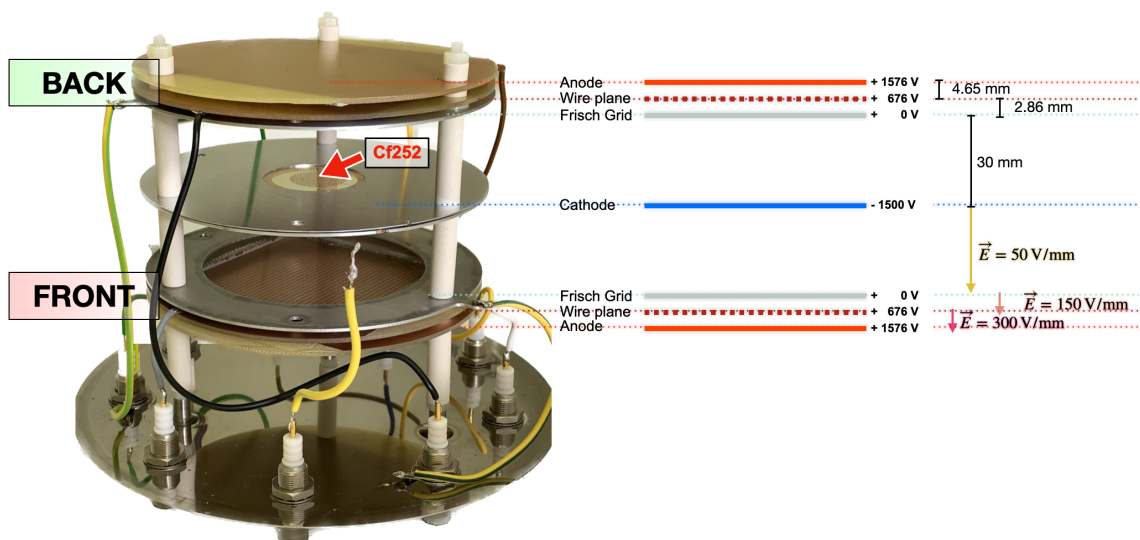
Figure 2.3: Interior and scheme with applied voltages and electric fields in the double Frisch-grid ionisation chamber.

The fissioning source, ^{252}Cf, is placed between the two aluminium disks, which are in contact with each other. The source placement in the centre of the detector allows simul-

taneous detection of both fission fragments, emitted in opposite directions, on both sides of the chamber, back and front. This centrepiece, the cathode, detects when spontaneous fission occurs, being crucial for timing resolution. Parallel to the cathode and three centimetres apart, the Frisch-Grids are placed on each side to prevent alpha particles from reaching the wire plane and anodes. No signal output is obtained from Frisch-Grids.

On the other hand, each wire plane and anode has two signal outputs, totalling, with the cathode, 9 output channels, see Fig. 2.4. It is possible to reconstruct the emission angle (in the x-axis or y-axis) by comparing the two output signals of the same component (wire plane or anode). The position figures per chamber side (back and front) can be reconstructed by the following relation, where P stands for the collected charge in the wire planes (P_1 and P_2) and A is the amplitude measured from the filtered signal of anode outputs (A_1 and A_2) and k_x and k_y are calibration constants[24].
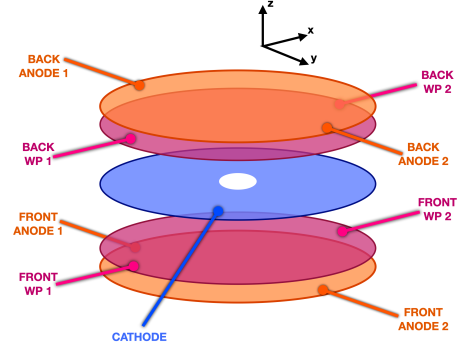
Figure 2.4: Scheme of ionisation output channels disposition.

$$\overline{x} = k_x \frac{P_1 - P_2}{P_1 + P_2}, \ \overline{y} = k_y \frac{A_1 - A_2}{A_1 + A_2} \tag{2.1}$$

Each IC chamber output goes through a preamplifier. Connected to the cathode, we have the CSTA2HV, a current-sensitive preamplifier suitable to HV up to 5 kV. This preamplifier has been chosen to improve the time resolution for the cathode channel. The other 8 channels of the IC have a charge-sensitive preamp, CSTA, suitable for up to 2 kV.

The voltages were set based on each chamber component's desired electric field strength. Between the cathode and the Frisch-grids, the electric field is chosen according to physical requirements on stable electron drift velocity and minimum recombination of electrons and ions in the gas.

The fission fragments ionise the gas, and this electron cloud drifts along the electric field created by the potential difference between the cathode and anode. The behaviour of such detectors is understood thanks to the Ramo-Shockley theorem that states: the charge Q and current i on an electrode induced by a moving point charge q is given by: $Q = -q\varphi_0(x)$ and $i = qv_0(x)$, where v is the instantaneous velocity of a charge q. $\varphi_0(x)$ and $E_0(x)$ are the electric potential and field at q's instantaneous position x under the following circumstances: the selected electrode at unit potential, all other electrodes at zero potential and all charges removed [25]. Consequently, the charge signals measured from the cathode are induced by the electron cloud movement rather than electron collection.

When alphas particles are emitted from the ^{252}Cf, they also ionise the gas, but since they have less energy, fewer electrons are liberated. Therefore, the amplitude of the

cathode signal generated from fission is higher than the cathode signal from an alpha decay, and it is possible to set a trigger threshold for the cathode signal, in this case at 44 mV, cutting off most of the alphas. In addition, the total activity of our ^{252}Cf is known, and from the tabulated branching ratios, we can evaluate an expected fission rate of ~ 800 fissions per second. With these parameters and triggering on the cathode signal, the DAQ counts around a thousand events per second from our fissioning source, including some α signals as a reference to confirm that the discrimination between the two types of signal is performed properly. Plus, if fission fragments are emitted, the 9 IC channels are triggered, adding to the detector selectivity.

The electric field between the cathode and the FG was set to 50 V/mm, resulting in an electron drift velocity of around 8 cm/μs for an internal pressure of 1.1 bar [18].

The remaining polarisation values are calculated to respect the desired field proportions. The field between the FG and the wire plane (WP) should be three times larger than the field between the cathode and FG, while the field between the WP and the anode should be twice as large as the field between FG and WP [24].

The IC can be filled with a noble gas to improve detection efficiency because the highly electronegative oxygen in the air easily captures free electrons, forming undesired negative ions. The usual choice is P10, a gas mixture of 90% argon and 10% methane. However, a pure methane bottle was chosen, bringing some advantages. With a pressure of 1.1 bar, the electron drift velocity in methane is larger than in P10, resulting in a better timing resolution and a drift time between the cathode and anode of 0.44 μs without gas flow. In comparison, for P10, we would expect around 1 μs in the same situation. The time resolution is essential because the cathode signal from an FF is considered the time zero of the fission event. The electrons' average drift time $\bar{t}$ and drift velocity $\bar{v}_d$ allow the reconstruction of the fission fragments' path along the z-axis following the equation 2.2, where $\bar{t}_0$ is the average drift time for FF emitted parallel to the source plane. The scheme of the gas circuit implemented is found in Fig. 2.6.
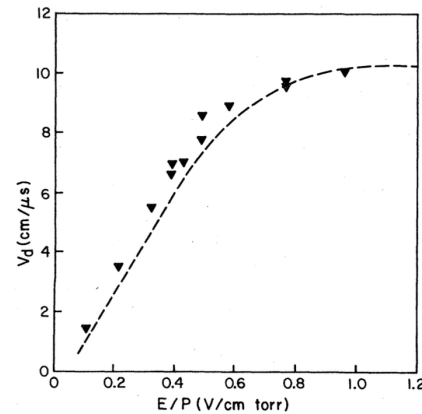
Figure 2.5: Electron drift time in methane *versus* voltage per centimetre for a pressure of 1 torr (1 bar corresponds to 750.06 torr). Taken from [18].

$$\overline{z} = \overline{v}_d \cdot (\overline{t}_0 - \overline{t}) \tag{2.2}$$

Gas circuit

This specific dFGIC operates with an internal pressure of 1.1 bar. We want a pressure slightly higher than atmospheric pressure because the internal gas will remain pure if there
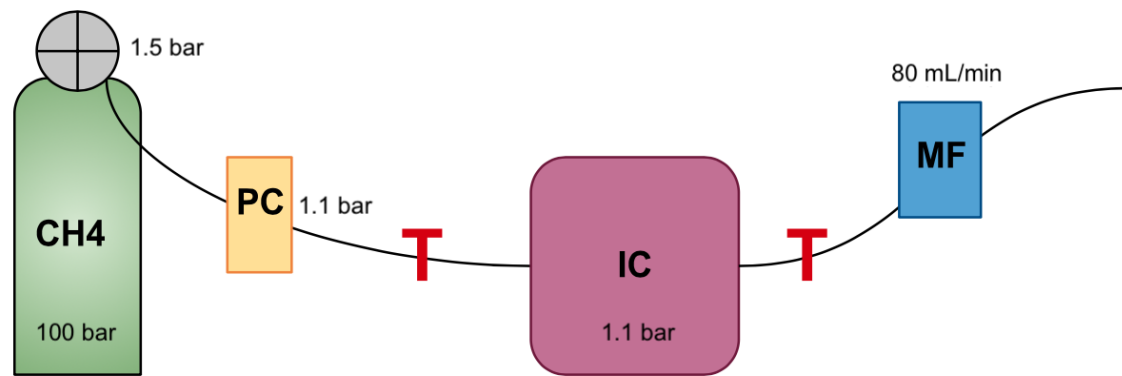
Figure 2.6: Scheme of the gas circuit on the ionisation chamber. The pressure controller (PC) sets the internal pressure on the IC to 1.1 bar, and the mass flow regulator (MF) sets an 80 mL per minute flow.

is a leak. In addition, gas-electric properties also depend on pressure. As a consequence, to ensure measurement repeatability, it is mandatory to maintain a constant pressure in the chamber. A gas bottle of methane with an internal pressure of 100 bar and output pressure regulated to 1.5 bar is connected to the pressure controller (PC). This device will set the internal pressure of the dFGIC to 1.1 bar. The second device connected to the dFGIC gas output is the mass flow controller (MFC). Indeed, because of the ionisation process that takes place in the chamber volume, the gas quality degrades over time. So, a rejuvenation is necessary. For this reason, the MCF is used to set a flow of 80 mL/min. The gas flowing out of the MFC is evacuated.

For all the reasons mentioned previously, we assumed that gas purity inside the chamber is insured only after 24 hours of gas flow. From that moment only, the polarisation should start.

Polarisation

After fully installing the ionisation chamber in our setup, the polarisation begins with the cathode. The voltage is increased slowly until it reaches the desired value because while the cathode signal baseline is somewhat stable while the voltage increases, the same does not apply to the other chamber components.

Polarising the anodes and wire plane requires more attention because the signal baseline also increases when the voltage increases. To avoid current discharges burning the preamps, the polarisation must be done slowly and carefully until the desired voltage is reached. Since the voltages are applied on both sides of each anode and wire plane, we built a tension splitter so both sides of the same component would have the same voltage and no unwanted current would be created.

2.1.3 FASTER data acquisition system

FASTER is a digital modular acquisition system developed at Laboratoire de Physique Corpusculaire (LPC) in Caen, France. It can handle various nuclear detectors with the same electronic boards, being suitable for νBall2 experiment setup, which comprehends 218 detector channels. Some of these detector types FASTER works with that interest us are HPGe, ionisation chambers and NaI, LaBr$_3$ scintillators with photomultiplier tubes.

For the ancillary detectors, we use the FASTER sampler acquisition module [6]. This module is designed for post-experiment personalised signal processing. It stores electronic signal frames with a maximum duration of 1428 ns, sampling the signal every 2 ns. This electronic signal we call trace, and the samples are the individual points that form the trace.

The sample amplitude is stored in arbitrary units (a.u.) that can be converted back to amplitude in mV (see conversion values in Table 2.1).

$$\text{sample}[i](mV) = \text{sample}[i](a.u.) \cdot \frac{2390}{2^n} \tag{2.3}$$

Table 2.1: **FASTER a.u. sample conversion to mV**

Signal amplitude (mV)	± 150	± 300	± 600	± 1200	± 2400
n	19	18	17	16	15
Detector	IC Wire Planes and Anodes	-	-	IC Cathode	Thalia

And the conversion from sample(mV) to sample(μC) in charge units is:

$$\text{sample}[i](\mu C) = \text{sample}[i](mV) \cdot \frac{1000}{50\Omega \cdot 2ns} \tag{2.4}$$

2.1.4 Remarks and challenges

Many adversities were faced during the campaign, and part of the job was identifying the problems and seeking solutions. It is also crucial to ensure the detectors' good operation, so some daily tasks had to be performed, such as keeping the germanium detectors at a cryogenic temperature.

HPGe clovers cooling system

The ν-Ball2 setup contains an automatic system for automatically refilling the HPGe every 6 hours, keeping them cooled during the experiment. Even though the HPGe clovers are automatically refilled with liquid N$_2$, the Dewar must be manually refilled every day. During the daily Dewar refill, it is a good practice to stay in the room during one of

the automatic refills to verify there are no leaks caused by broken tubes.

Polarisation

Special care is given to this polarisation step because some chamber parts are electrically segmented (anode and wire plane). These must be polarised in the very same way from both sides of the wires. A specific voltage duplication device has been built on purpose.

Electromagnetic compatibility and noise suppression

Many days were dedicated to the ionisation chamber installation in the setup, searching for better electromagnetic compatibility. The wire plane signals have an amplitude of a few mV, so the noise suppression must be good enough for the background noise to be less than 1 or 2 mV. The biggest challenge was the different groundings in our setup: the data acquisition system was placed in a separate room, so the detectors had different groundings (original ν-Ball and PARIS structures) than the DAQ. Minimising the background of the IC preamplifier output signals in the oscilloscope placed in the main room without checking the output connected to the DAQ could result in storing very noisy traces.

It was an iterative and very long process of trial and error, either connecting or isolating parts of the preamplifiers and their cables to get a signal with a more stable baseline and background noise with lower amplitude. We noticed that if the cathode preamp was not well grounded, the same noise behaviour could be seen in the other traces from the anodes and wire planes. The optimal solution was to isolate the preamp bodies from the ν-Ball structure with isolating tape and cover the connectors and preamp cables with aluminium foil attached to a flat braid of tin grounded to the original ν-Ball structure.

Electronic stability

After installing the chamber, the polarisation procedure follows the detailed instructions in subsection 2.1.2 at Polarisation. We faced many adversities until we completely polarised the chamber because there were many inadequate electronic parts in the setup, causing the preamps to burn repeatedly. The problems faced and their respective solutions are detailed below.

1. Sparks inside the detector:

Gaseous detectors are expected to have sparks inside them, creating unwanted currents capable of burning the preamps. Some of the welds inside the chamber had small peaks that could favour the creation of sparks once the detector was polarised. Some

were either remade or insulated with a Kapton tape, proper for electrical work and compatible with gaseous detectors. The cable connected to the cathode inside the chamber was inappropriate for HV, so it was replaced with a 9 kV - 50 CERN HV cable.

2. Avoid the creation of unwanted currents:

It is crucial to apply the same voltage to each side of each anode and wire plane to avoid unwanted currents. A simple voltage splitter is connected to each anode and wire plane high-voltage module output. If the voltage splitter receives an input voltage of V, each output also has a voltage of V.

Initially, that was not the case. For example, we would have back anode 1 (BA1) HV coming from one module and back anode 2 (BA2) HV coming from a different HV output from the same module. Even though both sides should be receiving the same voltage, small oscillations occur during the polarisation, creating an undesired current large enough to burn the preamp.

After implementing voltage splitters, the preamps would still burn during polarisation once we reached a specific voltage, so the search continued.

3. Inadequate cables:

Some cables used were improper for HV (1 kV standard signal cables), so the preamp would burn due to the very unstable signal the cable was conducting. Another simple circuit was built to check all the cables and verify their stability in HV, and new suitable cables were produced with 9 kV - 50 CERN HV cables.

A remark must be made regarding time consumption: just this last process took two working days during the campaign to build the voltage divider bridge box and the new cables. We were lucky enough to have the material at our disposal. Small problems meant one or more days without any data acquisition.

4. Unreliable power suppliers:

The first choice was to use the CAEN N1470 programmable high-voltage supplier module. This preamp has a very interesting feature as it allows the user to program the desired HV and how fast the voltage increases (ramp voltage). It seemed the best option because the polarisation could be done very slowly, steadily and reliably. Unfortunately, it was not as simple. Whenever the voltage reached 600 V, the preamp would burn. We only realised that the HV module was causing an unwanted current and burning the preamps when we took the module and a preamp to the electronic lab to ramp the voltage isolated from the rest. Even though this module had an overcurrent protection with the TRIP value (set to 0.000 s), whenever it reached 600 V, there was a discharge. The current limit

was set to its minimum of 0.5 mA, which is not small enough for the preamps' current sensitivity, or the overcurrent protection failed repeatedly.

The programmable module was replaced with the CAEN N471A high-voltage power supply. Due to the preamp's high sensitivity to the current, the HV module must have a great current monitor resolution of 1 nA. This module didn't present any anomalous behaviour. This module requires a manual voltage ramp, which brings a new difficulty since the anodes and wire planes must be polarised simultaneously, taking several minutes. In our setup, we have two 471A modules with 2 channels each. One module is reserved for the anodes, and the other is for the wire planes. A voltage splitter is connected to each module output.

5. Unstable crate:

After replacing the unstable modules, we noticed a malfunction on the crate, replaced by a Wiener high-power crate. The problem was a randomly occurring fluctuation on the crate low-voltage (11V instead of 24V), limiting the voltage delivered by the module.

Finally, all the preamp failure causes were eliminated.

Once the broken preamps were fixed, we successfully polarised the complete chamber at the beginning of the campaign's third week. Ideally, there should have been one or two weeks of tests and preparation before the beginning of the experience. Still, the ionisation chamber was not yet available, so we had only three days, clearly not enough to rule out all of the problems encountered.

Acquisition system

The FASTER acquisition system presented some issues, and the configurations had to be altered many times. To reduce the amount of data, FASTER has a group option, where it only saves the data from certain channels to disk if a condition is satisfied. The idea was to store the traces only when the 9 channels of the IC were triggered. The event count was much lower than expected, and most traces didn't have a proper signal.

To avoid losing more precious experiment time, we decided to run trigger-less. It means each trace itself has its own trigger, but no group is formed.

One of the recommendations from David Etasse, FASTER developer, was to set a threshold and validation level very close to one another, or even the same. The validation level means that the voltage remains higher than a specific value for a few nanoseconds (set according to the signal behaviour). Both threshold and validation levels were set to 44 mV on the cathode signals, a threshold capable of cutting out most of the alpha particles. The anodes and wire plane signals were harder to trigger, so we devised a solution: using a linear FAN-IN/FAN-OUT module, we replicated and delayed the cathode signal and used

them to trigger the acquisition of the anodes and wire plane traces. Instead of only 9 IC channels of type samples, we had 18 channels (counting the LaBr$_3$ THALIA, for high precision timing resolution):

- 1 channel for cathode;
- 4 channels for anodes;
- 4 channels for wire planes;
- 8 channels for delayed cathode signals;
- 1 channel for THALIA;

In some of the initial runs, we had a lower threshold and validation level, so many traces from the alpha particles were stored. All of the figures presented in this work were obtained from the data coming from the trigger-less runs with a threshold of 44 mV.

To have trigger-less data means that the analysis becomes much more complex and time-consuming because we have to, later on, select the real events. For an event rate of between 800 events/s and 1000 events/s at FASTER (depending on the parameters of each run), the event count from our own algorithm triggered only 300 events/s. This count rate was verified with different approaches, and my supervisor, M. Lebois, and I converged to the same value.

Chapter 3

Analysis method

This chapter presents the procedure chosen for trace analysis to be later compared with the artificial intelligence approach. Independently from the analysis technique chosen, there is an interest in performing a trace analysis for the ionisation chamber signals to improve the timing precision and to calculate the electrons' drift time in the anodes to determine the third coordinate (z-axis).

The FASTER data acquisition system with CARAS cards (500 MHz, 12 Bits) can save signal samples with a resolution of 2 ns, but we aim for better precision. Through Constant Fraction Discrimination (CFD) and evaluation of the zero crossing in the cathode traces, we find the time zero, t_0, of each fission event with a precision smaller than 1 ns. FASTER can perform this CFD calculation thanks to CARAS card specifications. However, FASTER cards are not able to perform other mandatory operations for anode and wireplane signals. Also, FASTER is not programmed to calculate the electrons' drift time.

The amplitude units of the traces can be reconstructed in mV.

3.1 Trace analysis

From the traces, we want to measure the time of the interaction and energy deposited. The signal from different parts of the ionisation chamber has different behaviours; therefore, various signal processing techniques are used in each case.

Each technique requires identifying adequate parameters that improve energy and time resolution. That is one of the challenges of trace analysis: combining the search for optimal parameters with a long computing time.

Another challenge regarding the trace analysis is performing the correct technique adjustments for your own data and setup.
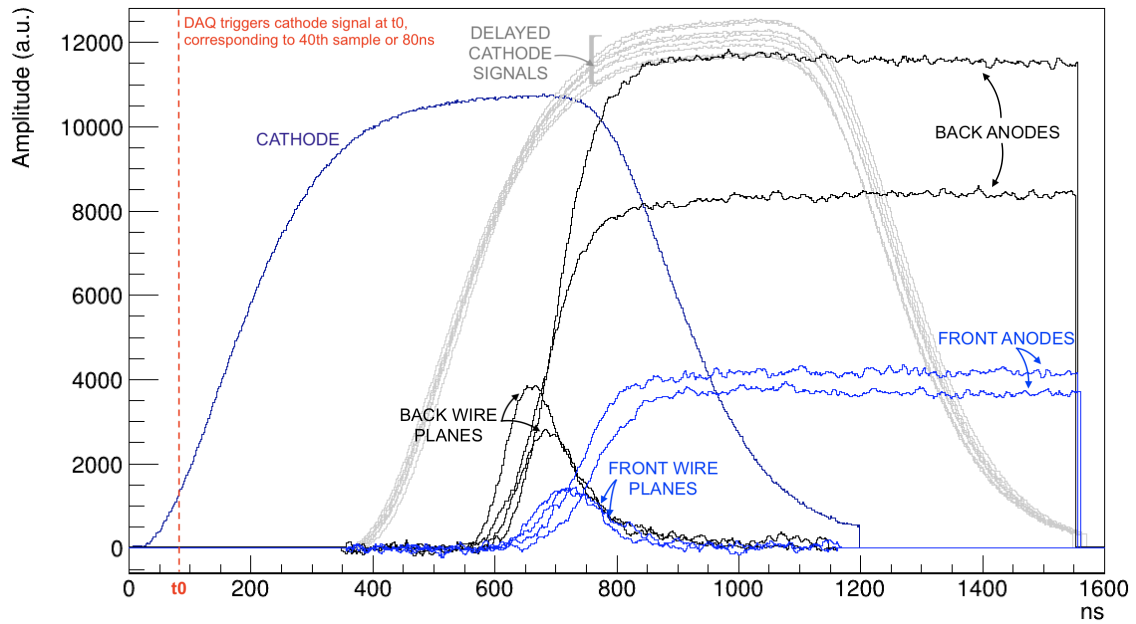
Figure 3.1: Ionisation chamber traces for one fission event aligned in time. The conversion factor from arbitrary units (a.u.) to mV is $\frac{2390}{2^x}$, where $x = 16$ for the cathode and delayed cathode traces, while for the other traces, $x = 19$.

3.1.1 Moving average algorithm

Despite the many hours dedicated to noise suppression, our traces have some high-frequency background noise. Therefore, we applied a low pass filter: a moving average algorithm.

Besides the traces, the other input for the moving average function is the number of samples. This number is directly related to the time constant in a conventional low-pass filter. The best approach is to observe several samples and use twice the noise period as the time constant. This time constant is considerably smaller than the signal rise time, so we filter the signal from its background.

The low pass filter is always applied in our trace analysis to avoid erroneous measurements, such as finding a wrong zero crossing with CFD due to small background noise peaks.

3.1.2 Signal offset

The curve offset algorithm corrects fluctuations on the signal baseline for a more precise measurement. Our IC traces have a positive polarity, but due to background noise oscillations, some points could be negative. This algorithm will keep only positive values. This last step is more relevant in the wire plane energy analysis because we integrate the deposited charge.

3.1.3 CR-RC and CR-RC4 filters

The anode signals pass through a digital signal processing algorithm simulating CR-RC or CR-RC4 filters. They serve as semi-Gaussian shaping amplifiers, producing a signal with an amplitude proportional to the energy deposited by the FF in the counting gas. The scaling factor is set to align the spectrum of the two sides of the same anode and amplify the signal that loses amplitude after passing through the filters.

One of the perks of a position-sensitive ionisation chamber is to reconstruct the fission fragments' emission angle. To preserve the position sensitivity, the shaping time for the position signals must be kept shorter than the charge redistribution time constant.

3.1.4 Signal integration

The wire plane signals have a very small amplitude of a few mV, a strong reason why good noise suppression was essential. To obtain the deposited energy, we perform a simple charge integration of the signal with baseline correction and moving average algorithm to reduce the noise.

Since the trace values correspond to the signal amplitude (mV), we must convert to charge deposited before integrating. We obtain the current measured from Ohm's law $V = RI$, where $R = 50\Omega$. Dividing it by the bin size (2 ns), we obtain the induced charge.

3.1.5 Constant Fraction Discrimination (CFD)

The constant fraction discriminator is an electronic signal processing device used for triggering signals more reliably compared to a simple threshold voltage. In this context, we are not using an electronic device; we implement a function miming a standard CFD in our code. The standard CFD step-by-step is as follows:

- Invert the original signal and reduce its amplitude by a factor of 3 (some authors recommend 5). Since our samples are obtained every 2 ns, the default values for the factor in the FASTER acquisition system are 2, 4 and 8.
- Subtract this modified signal from the original signal delayed by t_d, where t_d is smaller than the signal rise time.
- Find the zero crossing between the minimum and maximum of the final curve.
- With the zero crossing sample and its two previous and following samples, calculate a second-order polynomial interpolation[1] for a zero crossing with precision under 1 ns.

Since we are working with samples, a good way to choose t_d is by guaranteeing that the peak right before the zero crossing can be identified; in other words, it has at least

---

[1]Second-order polynomial interpolation, also known as quadratic interpolation, is a mathematical technique used to estimate the value of an unknown point within a set of data points. In the context of your signal processing, it is employed to enhance the resolution of zero-crossing detection.

3 points. The t_d was chosen to obtain a more precise zero crossing (trigger), hence, a better time resolution (below 2 ns).

3.2 Event Reconstruction

To reconstruct an event, first, we must define what characterises our event. Our fission event occurs when we detect fission fragments in our ionisation chamber. Therefore, we should have positive signals on both sides of the IC.

Indeed, there could be alpha pile-ups, and this correction should be done further in the analysis. In the scope of this thesis, where the focus is on the analysis techniques of the traces, such correction won't take place.

Simplifying the iterations in event reconstruction, the process starts during the data acquisition with a preliminary selection of events and a complete cathode and Thalia trace analysis (spectrum and trigger time from CFD for both). From the time-of-flight figure between the cathode and Thalia, we obtained a preliminary time resolution of our setup. Anodes and wire plane spectrum for each channel are plotted to verify that all channels are working properly.

At the end of the experiment, all the analysis must be done from the beginning with much more careful thought, especially because we aim for high-precision measurement. All the parameters used during the trace analysis are chosen based both on our references and the characteristics of our traces, and they need to be tuned carefully to improve the results. Due to the dependence between these parameters, the event reconstruction is a long, complex and iterative process.

For clarity, this section was not written in chronological order, except for the first subsection 3.2.1 Data screening; instead, I decided to present the analysis of each component independently at first.

3.2.1 Data screening

Ideally, we could have used the FASTER grouping acquisition option and CFD triggers in each channel; this process would've been straightforward since FASTER grouping does a pre-selection of the traces that will be stored. However, that is not our situation. As mentioned, our acquisition was without group selection and based on an amplitude threshold. Besides that, the trigger is always done with cathode or delayed cathode signals. In other words, even though we find anodes and wire plane signals stored, many of them are only background noise since we store them whenever the delayed cathode passes the threshold (see Fig. 3.2).
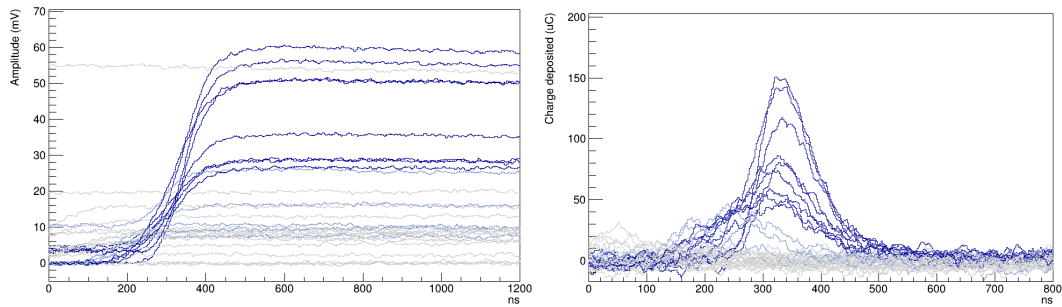
Figure 3.2: Various anodes (left) and wire planes (right) raw traces. The colours are set based on measured amplitude for better visualisation. Darker colours mean higher amplitude traces. Anodes amplitudes are converted to mV and wire planes in deposited charge μC.

Even the cathode traces, triggered with a 44 mV threshold, have useless signals due to a late trigger during trace decay for smaller amplitude traces. In Fig. 3.3, many cathode traces are plotted with different colours based on their amplitude. The smaller the signal, the higher the baseline appears to be, but looking at the decay, the traces always converge to zero. Hence, the late trigger is due to the signal shape reaching its maximum amplitude around 700-800 ns.
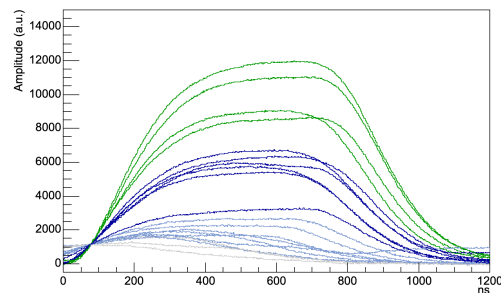
Figure 3.3: Various cathode traces. Amplitude is in FASTER arbitrary units (a.u.), to be converted later to mV. The colours are based on measured amplitude for better visualisation.

Preliminary selection of events

To identify an event, we must read all the data and measure the deposited energy. If the 9 channels have a positive energy value higher than the FASTER setup threshold, for now, we consider we have an event for a preliminary measure of event count. With this approach, we estimate 740 events per second. This event count must be refined with energy and time measurements for the proper identification of our fission events when fission fragments are identified.

3.2.2 Cathode trace analysis

The most important parameter from the cathode trace is the trigger time, which should be calculated through CFD. The cathode t_0 is the fission tag of the whole ν-Ball2 setup, so we aim for a time resolution under the 2 ns of FASTER resolution.

For both energy and time measurements, the raw signal passes through a moving average algorithm, followed by measurement of the baseline for baseline correction (Fig. 3.4).

The cathode signal amplitude is energy and angle-dependent, while the rise time

Table 3.1: **Cathode parameters for first treatment**

Moving average number of samples	Baseline number of samples
20	20
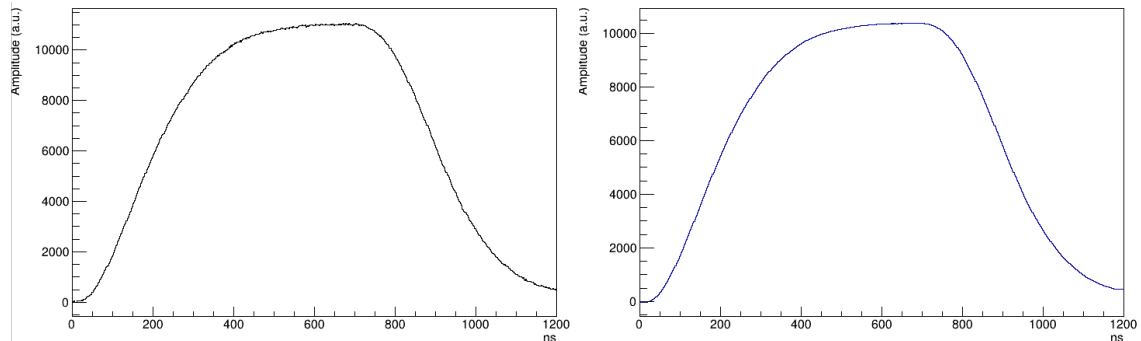
Figure 3.4: Cathode raw signal (left) and cathode signal after moving average low-pass filter (right). Amplitude in arbitrary units (a.u.).

is angle-independent [23]. From the initial screening, we identified the storage of what seems to be incomplete cathode signals that pass the FASTER threshold very close to the signal maximum. Since the sample is long enough to have the complete fall of the cathode signal, we can compare the rise time[2] *versus* amplitude with the decay time[3] *versus* amplitude to verify our theory. Due to our cathode signal rising shape for both rise and decay time, we measure the time difference from 20% to 80% of the signal amplitude before and after the maximum. This measurement is conditioned to the sample precision of 2 ns.
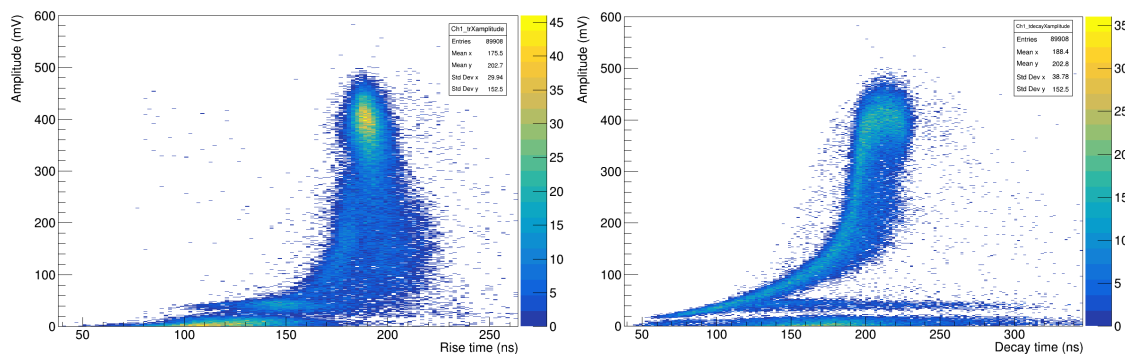
Figure 3.5: Cathode amplitude *versus* rise time and cathode amplitude *versus* decay time.

Indeed, in Fig. 3.5, in the rise time graph (left), we observe a more scattered measure of rise time for lower amplitudes, while the behaviour for the decay time graph (right) better follows the same behaviour. The rise time of the signals is somewhat stable around 200 ns except for much lower amplitudes, which can indicate an improper trigger of the trace.

---

[2]The rise time is the time taken for a signal to cross a specified lower voltage threshold followed by a specified upper voltage threshold. Usually, the thresholds are set to 10% and 90% of the signal maximum amplitude.

[3]Decay time or fall time, analogously to the rise time, is the time taken for a signal to cross a specified upper voltage threshold followed by a specified lower voltage threshold.

For future experiences, there are a few options to avoid losing the beginning of the trace. If possible, the most reliable way is triggering the cathode with CFD, which is not possible for the sampler acquisition mode. Another solution is to decrease the threshold level at the cost of storing an immense amount of data from alpha particles unless the FASTER grouping is activated with a threshold implemented for each IC component.

Time

After the moving average and baseline correction, the CFD can be directly applied to the cathode signal. With this approach, the time resolution was very poor, higher than 20 ns. Therefore, a CR-RC4 Gaussian shaping filter was applied to the cathode trace, and the best time resolution was found for a shaping time of 200 ns and a time delay of 25 samples.

Table 3.2: **Cathode parameters for trigger time determination**

CR-RC4 shaping time	CFD number of delayed samples	CFD fraction
200	25	2

The time resolution is obtained by analysing the gamma time-of-flight peak between the cathode and another detector (Thalia). This topic is discussed in subsection 3.2.9.
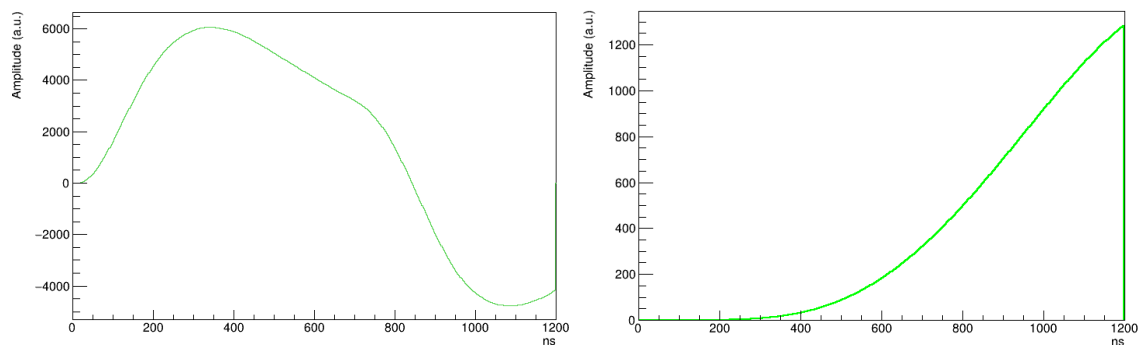
Figure 3.6: Cathode signal after high-pass CR filter (left) and cathode signal after 4 consecutive RC low-pass filters (right). Amplitude in arbitrary units (a.u.).

In Fig. 3.4, Fig. 3.6 and 3.7, the behaviours of the cathode trace after each step are presented. It is expected to have the CFD zero crossing after sample 25 (or 50 ns), corresponding to the delay chosen.

The crossing zero is not simply 84 ns but between 82 and 84 due to the second-order polynomial interpolation. We obtain a trigger time with a resolution better than 2 ns.
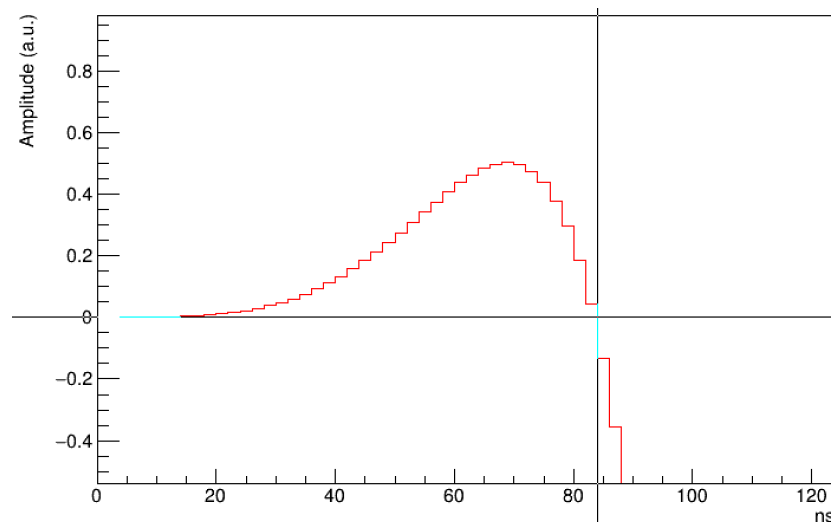
Figure 3.7: Cathode signal after CFD. Zero crossing for this trace occurs in sample marking 84 ns. Amplitude in arbitrary units (a.u.).

Energy

Since the cathode signal has a well-defined shape and most of the noise can be reduced with the low pass filter, no other filter needs to be applied to improve the signal-to-noise ratio.

For the amplitude measurement, I wrote an algorithm that follows a similar train of thought as Newton's method, or gradient descent. A simple iteration to find the maximum of the curve would require 600 iterations (total of samples); while implementing this gradient descent method, the maximum value converges with around 30 iterations, a relevant improvement on computational cost. It can only be used in the cathode traces because it doesn't have local maximums other than the true maximum value. Briefly, it works as follows:

Figure 3.8: Cathode traces following energy procedure with amplitude measured in mV. Raw signal (higher in amplitude) and signal after moving average algorithm.

- First guess of curve maximum as the middle sample;
- Calculate the derivative at the current guess;
- Update the guess to converge to gradient zero;
- Repeat.

Comments

For visualisation purposes, the Fig. 3.9 traces are plotted with different colour codes depending on the trace amplitude. The threshold values were chosen based on the cathode
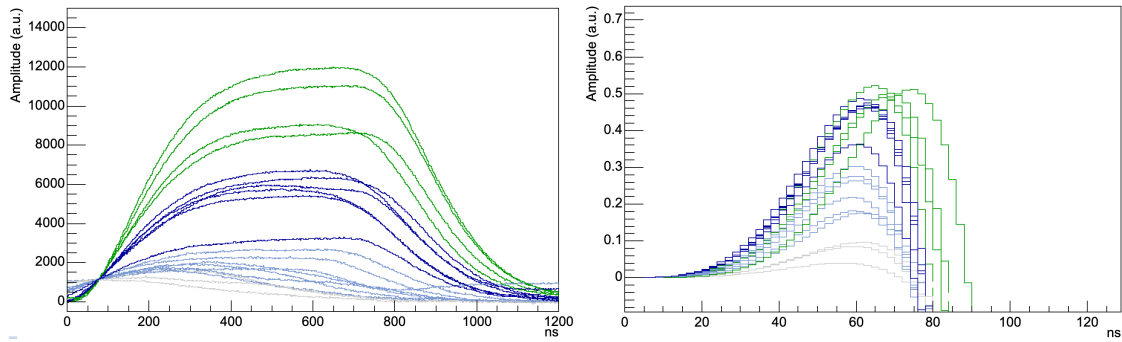
Figure 3.9: Canvas with various cathode raw signals (left) and the same traces after applying the CFD (right).

spectrum, presented later in subsection 3.2.8 in Fig. 3.17. If the colours are not visible to the reader, the relevant parameters read from the plot are found in Table 3.3.

Table 3.3: **Complement to Fig. 3.9**

Threshold a.u.	Threshold mV	$<t_0>$ns	colour
8226	300	84	green
2056	75	78	dark blue
1206	44	76	light blue
-	-	70	grey

This display is very important to conclude on the quality of the CFD. On analogical electronic CFDs, we expect the crossing zero to be all aligned because the CFD is a trigger method independent of the signal amplitude, and only 3 positive samples before the zero crossing would be enough. This is clearly not the case in Fig. 3.9. The sample numbers are not independent of trace amplitude because we have a trigger based on amplitude threshold; hence, it is not unusual to find zero crossings at different positions for traces with different amplitudes. Also, the number of delay samples was set to a higher amount of 25 samples or 50 ns, which increases the number of samples before the trigger. On the other hand, this value was chosen after analysing the variance of the zero crossing, also trying to optimise the energy resolution of the cathode signal with the gamma time-of-flight between the cathode and Thalia detector (to be explained later) converging to a delay of 25 ns.

3.2.3 Anode trace analysis

From the anodes, we want to obtain a good energy resolution on the anodes' spectra to reconstruct the fission fragments' energy and the electron drift time to reconstruct the FF emission angle (discussed in subsection 3.2.10).

Both the energy and drift time of anodes are calculated from the total signal of the back anode and the front anode. This means the signals from each side of the same anode must be added, also improving the signal-to-noise ratio. A pre-processing of the anode traces of one fission event must be done.

Firstly, the energy procedure should be performed without adding the traces because the channels are not perfectly calibrated in energy. By plotting one spectrum for each one of the four anodes, the peaks can be aligned. This scaling factor is very important; Without it, one side of the same anode will, on average, have higher signals than the other, bringing uncertainties to the drift time calculation and decreasing the energy resolution on the spectrum, hence worsening the FF mass separation in further analysis. Secondly, the trigger time is crucial for correctly aligning the traces for energy and drift time calculation since they are not triggered on themselves but by a cathode-delayed signal.

For both energy and time measurements, the first step is to apply a moving average algorithm followed by a baseline correction.

Table 3.4: **Anodes parameters first treatment**

Moving average number of samples	Baseline number of samples
40	40
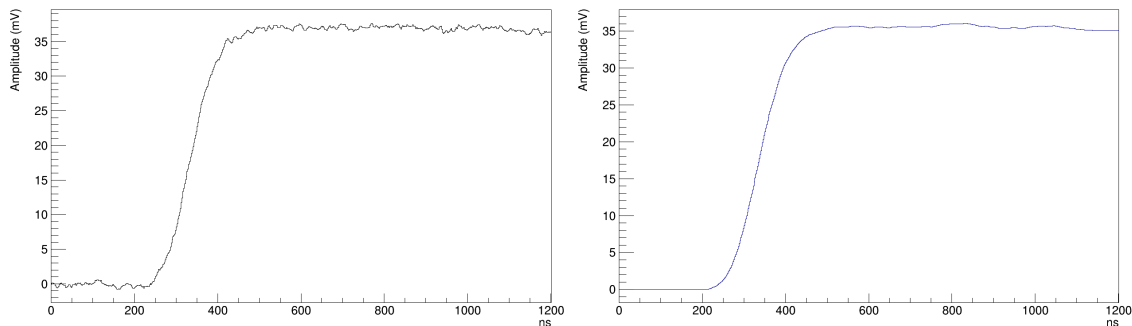
Figure 3.10: Raw anode trace (left) and anode trace after running mean and baseline correction (right). Amplitude measured in mV.

In both time and energy measurements, the anode trace passes through a CR-RC4 shaping filter. To capture rapid changes in the signal, a shorter shaping time is ideal, and to smooth out variations and reduce noise, a longer shaping time is more suitable. The values chosen and the reasoning for time and energy are explained in the following subsections.

Time

The best approach to define the trigger of each anode trace is by applying a CFD after shaping them with CR-RC4, which should capture the signal rising.

Table 3.5: **Anodes shaping time for trigger time**

CR-RC4 shaping time	CFD number of delayed samples	CFD fraction
50	40	2

Energy

According to A. Göök et al. reference article [24], where the same ionisation chamber was used, the anodes' signals are shaped with a CR-RC4 filter to obtain the best energy resolution and reduce the signal-to-noise ratio.

To measure the deposited energy, we should choose a shaping time that comprehends the rise time and part of the decay of the signal.

Our reference has used a shaping time of 10 μs, but their anode traces were 6μs long (Fig. 3.11) while ours are 1.2, having much more trace information, while we don't have much information on the decay. If we apply a huge filter of 10 μs on our 1.2 μs samples, we will have a filtered trace of zero amplitude. To remediate this situation, we implemented a decay compensation algorithm in our anode traces decay portion and extended them.
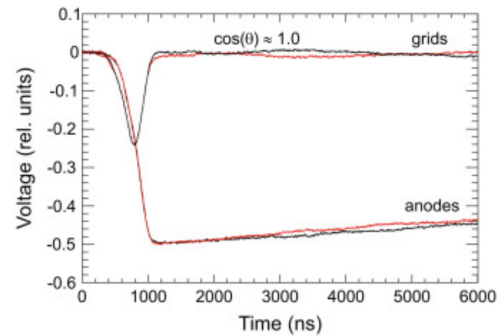
Figure 3.11: Reference IC traces taken from A. Göök et al. [24]. Grids stands for wire plane signal.

With a decay constant of 72.4 μs for the anodes' preamp signal, we can compensate for the decay, obtaining a signal that resembles a step. We calculate the average value from the last n compensated samples and extend our samples by adding other 5k samples at the end with that average value.

Now, the compensated-topped traces are suitable for the CR-RC4 filter.

With the extension on our sample, the shaping time can be safely increased up to 1 μs (see Fig. 3.12). For higher shaping times, the maximum position in time of the filtered trace is higher than the total of samples, becoming impossible to measure. Indeed, we could extend the samples even more than 10 μs, but the computational cost increases drastically. With 1 μs shaping time, we are focusing on the part of the signal acquired and not the prediction part.

Table 3.6: **Anode parameters for energy determination**

Number of compensated samples	CR-RC4 shaping time
5000	1000

I choose to stick with this decision throughout the analysis for the reasons mentioned above. The step-by-step of the anode trace analysis is exemplified with a trace from the back anode 1.

The energy value is the maximum of the final filtered signal.
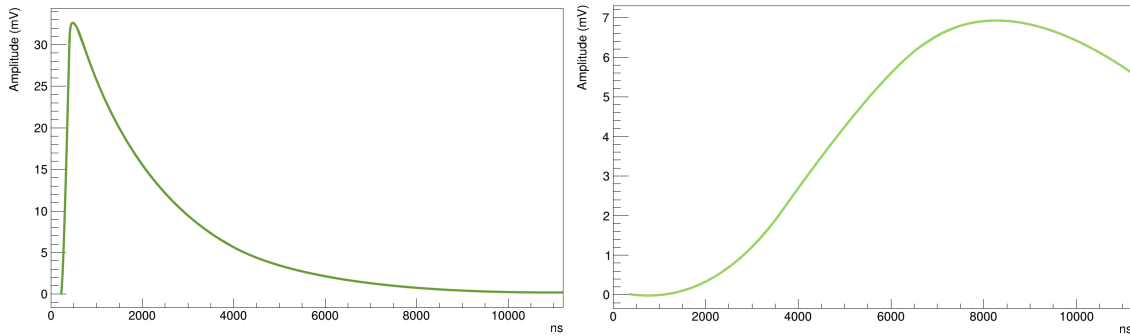
Figure 3.12: Extended anode trace after high-pass CR filter (left) and then after 4 consecutive RC low-pass filters (right). Amplitude measured in mV.

Comments

After finding the scaling factors and the time trigger, the energy procedure is repeated for the total back anode and total front anode raw trace.

The scaling factors used to calibrate the anode traces between themselves are presented in Table 3.7.

Table 3.7: **Anode (An) scaling factor for energy calibration**

	Back An1	Back An2	Front An1	Front An2
Scaling factor	0.7777	0.9531	1.2180	0.9991

The raw trace is the sum of the raw traces of the same anode (e.g. back anodes 1 and 2), aligned and with the correct scaling factor. The alignment does not mean considering the triggers as the same. It means reconstructing the true time of the signals and adding the traces with the correct delay between them, if any.

3.2.4 Wire plane trace analysis

The wire plane is relevant for reconstructing the emission angle of the fission fragments through the deposited charge. The angle can be reconstructed with the ratio between the deposited charge measured on each side of the same wire plane (discussed in subsection 3.2.11).

To exemplify the wire plane traces analysis, we have a raw signal obtained from back wire plane 1 (channel 4). A moving average algorithm is very important to reduce the signal-to-noise ratio and to correct the baseline.

Table 3.8: **Wire plane parameters first treatment**

Moving average number of samples	Baseline number of samples
20	20
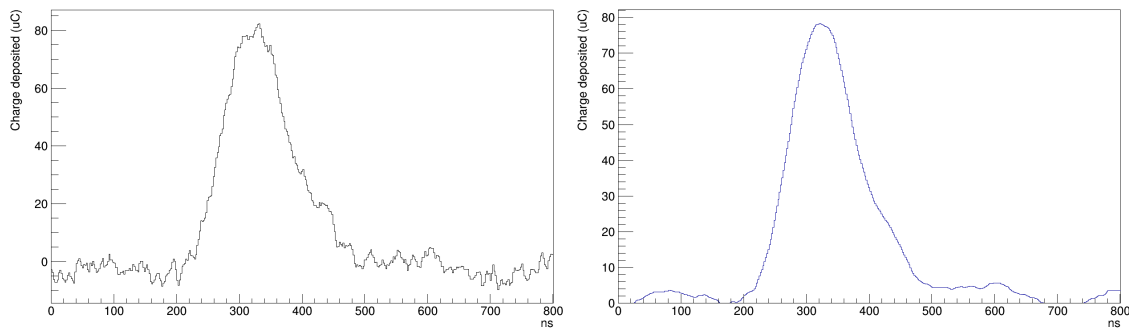
Figure 3.13: Raw wire plane signal (left) and wire plane trace after moving average and baseline correction (right). Amplitude is measured in μC.

Time

To obtain a trigger time for wire plane traces, besides the moving average and baseline correction, one can apply a CR or CR-RC filter before the CFD. The shaping time should be around the rise time of the signal to avoid losing much amplitude but still improving the signal-to-noise ratio. A good start for the delay time is to set a couple of samples, such as 3 to 5 and evaluate the behaviour of the CFD.

Since a precise trigger time measurement of the wire plane signal is unnecessary to characterise the fission events, and we aim to minimise the computing time, this step was skipped in the final analysis.

Energy

Therefore, the energy of the wire plane is measured by the integral of the peak. This process should be done twice to calibrate the wire plane channels' energies between themselves, as we did with the anodes. The wire plane sample values are converted to charge to integrate the deposited charge. No sample should have a negative value. If so, it is set to zero before integrating. The integration of the discrete traces is straightforward, being the value (amplitude) of each individual sample times the bin size of 2 ns.

Comments

The scaling factors used to calibrate the wire plane traces between themselves are presented in Table 3.9.

Table 3.9: **Wire plane (WP) scaling factor for energy calibration**

	Back WP1	Back WP2	Front WP1	Front WP2
Scaling factor	0.9555	0.8186	1.0000	0.9141

3.2.5 Thalia trace analysis

The motivation for storing Thalia traces instead of letting FASTER perform its own CFD is to obtain a trigger time reconstruction more precise than FASTER zero crossing recon-

struction with CFD and evaluate the use of sampler acquisition mode in LaBr$_3$ detectors for time resolution improvement.

The time resolution is determined by the FWHM[4] of the time-of-flight peak between the cathode and Thalia. To evaluate the quality of the TOF, we compare it to the time coincidence peak of Thalia and one of the PARIS phoswhiches.

The complete analysis of Thalia's traces involves the analysis of a run with the ionisation chamber with a ^{252}Cf and another run without the ionisation chamber with a spontaneous fissioning source of ^{60}Co and ^{137}Cs with a much higher gamma activity for gamma coincidence peak detection.

Even though we look for Thalia's trace trigger time, we should also read Thalia's spectrum so we only count the gammas from the fission event.

Table 3.10: **Thalia parameters first treatment**

Moving average number of samples	Baseline number of samples
10	1
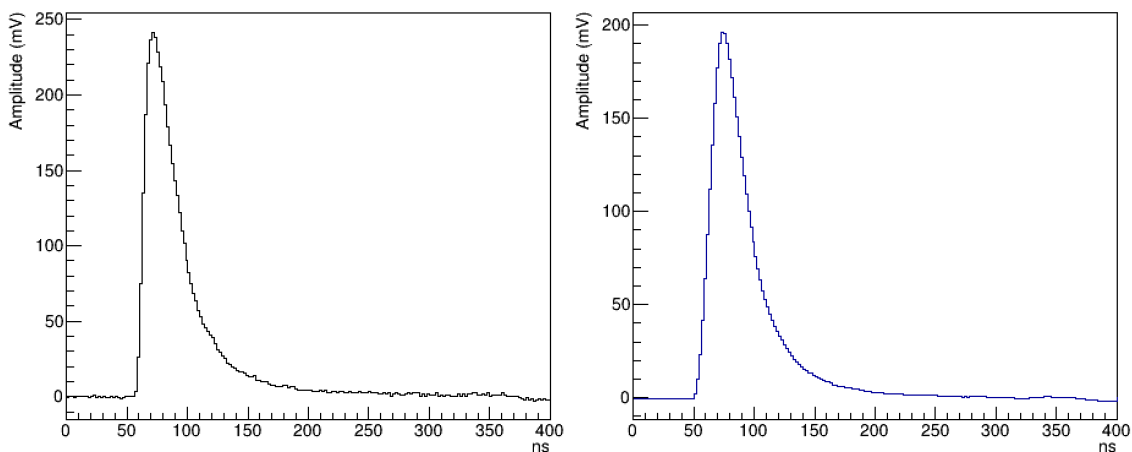
Figure 3.14: Thalia raw trace (left) and trace after moving average and baseline correction (right).

Energy

Thalia trace energy was estimated by measuring the signal's maximum amplitude after the moving average algorithm and baseline correction.

Time

The time trigger of Thalia is done through CFD. Due to the very short rise time, the CFD is performed with a delay of 6 ns, reproducing the delay used for PARIS detectors' CFD trigger.

---

[4]In a distribution, full width at half maximum (FWHM) is the difference between the two values of the independent variable at which the dependent variable is equal to half of its maximum value.

The fraction value had to be adapted; while for PARIS, the fraction was set to 2, this value created a discontinuity in Thalia zero crossing analysis. The fraction that minimises this discontinuity is 5, counterintuitively since FASTER uses fractions multiples of 2: $\frac{1}{2}$, $\frac{1}{4}$, $\frac{1}{8}$.

With these parameters, we find a zero crossing coherent with a variation of only one sample (2 ns), Fig. 3.15.
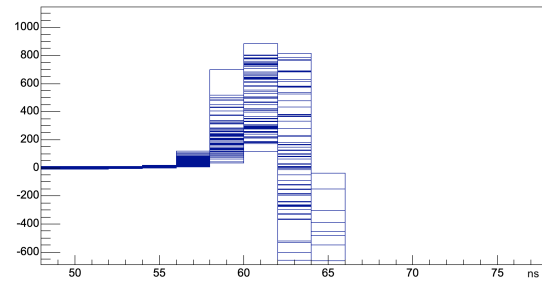
Figure 3.15: Many Thalia CFD traces in the same canvas to evaluate CFD quality.

Table 3.11: **Thalia parameters time trigger**

CFD delay number of samples	CFD fraction
6	5

Comments

In some of the experiment runs, the inhibition gate for Thalia traces acquisition was set to zero, and as a result, some low amplitude traces were triggered twice. In the analysis, verification of traces is also performed to neglect the second trigger of the exact same trace, as Fig. 3.16 shows.
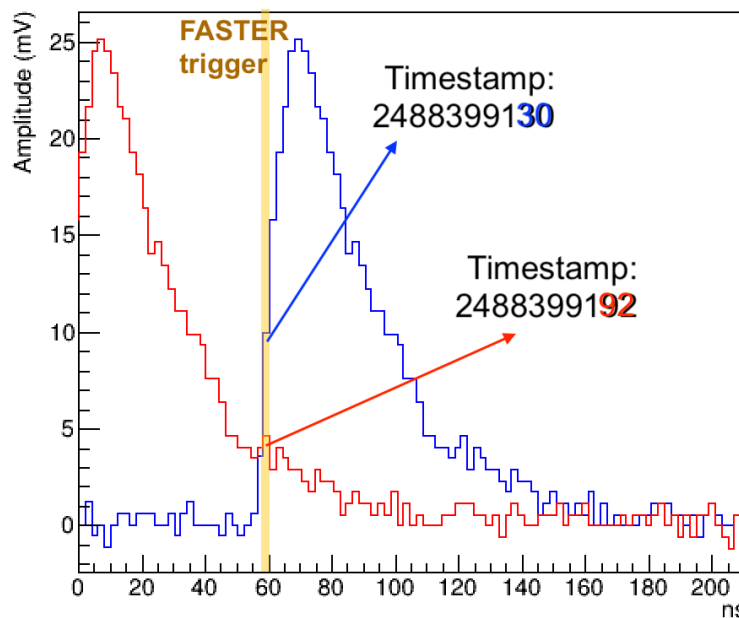
Figure 3.16: The FASTER sampler correctly triggered the blue trace (centred around 80 ns), but then, 62 ns later, the exact same trace is triggered again due to a small noise peak during the decay, red trace (centred around 10 ns).

From 3.15, it is also possible to conclude that the traces wrongly triggered were correctly neglected.

3.2.6 Summary of time procedures

The time analysis procedure of each component is summarised in Table 3.12.

Table 3.12: **Summary of trigger time determination procedure**

COMPONENT	Ch.	Moving average	Signal offset (baseline)	CR filter	RC4 filter	CFD delay	CFD fraction
CATHODE	1	40 ns	40 ns	200 ns	200 ns	24 ns	2
ANODES	2, 3, 6, 7	80 ns	80 ns	50 ns	50 ns	50 ns	2
WIRE PLANE	4, 5, 8, 9						
THALIA	725	10 ns	2 ns			6 ns	5

3.2.7 Summary of energy procedure

The energy analysis procedure of each component is summarised in Table 3.13.

Table 3.13: **Summary of energy determination procedure**

COMPONENT	Ch.	Moving average	Signal offset (baseline)	CR filter	RC4 filter	Amplitude measurer	Inte-gration
CATHODE	1	40 ns	40 ns			x	
ANODES	2, 3, 6, 7	80 ns	80 ns	1000 ns	1000 ns	x	
WIRE PLANE	4, 5, 8, 9	40 ns	40 ns				x
THALIA	725	10 ns	2 ns			x	

3.2.8 Spectra

The energy spectra obtained from the energy procedures are presented here.

Cathode
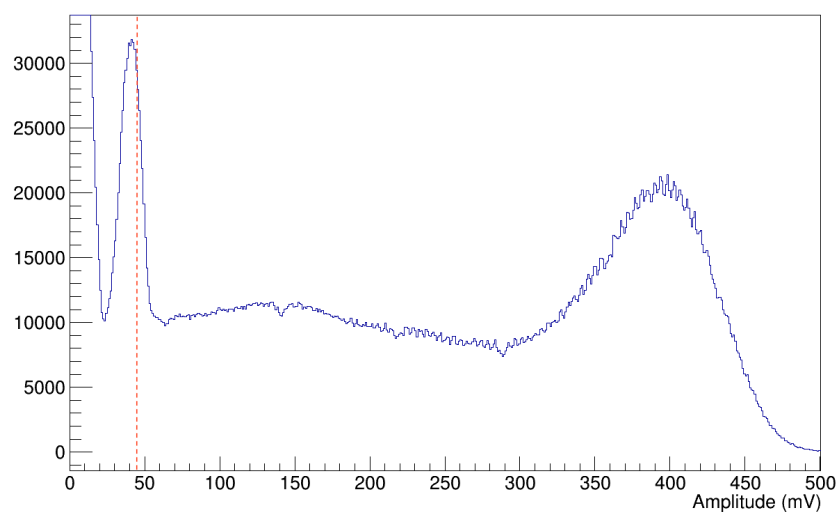
Figure 3.17: Cathode spectrum.

The red dashed line limits the 44mV threshold set on the DAQ FASTER (Fig. 3.17).
Due to the moving average algorithm, it is normal to measure some traces with energies

below that threshold. The traces with measured amplitudes below 25 mV before the first peak can be discarded.

The broad peak centred at 400 mV corresponds to 36 % of the total spectrum integral. The corresponding event rate is 340 events per second.

Anodes
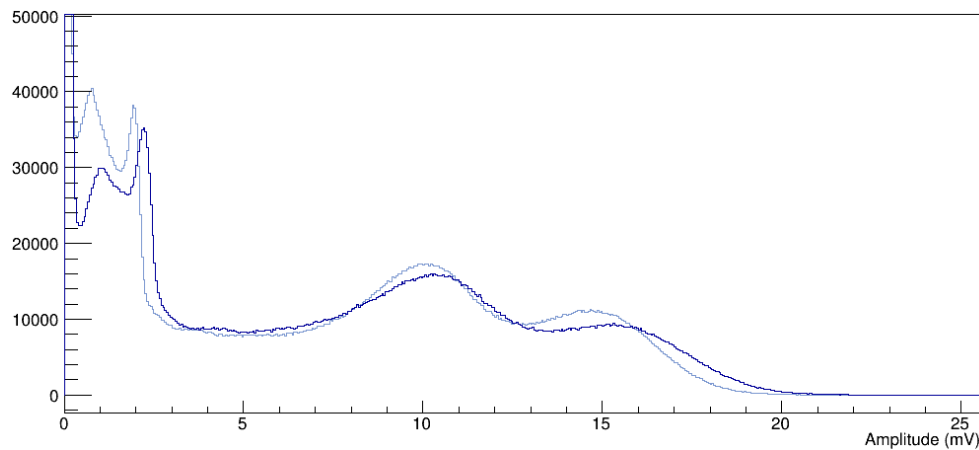
Figure 3.18: The lighter spectrum refers to the back anode, and the darker line is the front anode spectrum.

The spectrum obtained from the anodes' traces is presented in Fig. 3.18. There is a clear separation of fission fragments' mass: the peaks around 10/11 mV correspond to the light fragments, and the peaks around 15/16 are the heavy fragments.

If we compare the integral of the broader peak centred around 400 mV on the cathode spectrum with the two peaks around 13 and 19 mV on the anode spectrum, we notice they correspond to roughly 40% of the total entries. So, instead of 700s events per second, we only measured around 300 events per second (fission fragments).

Thalia
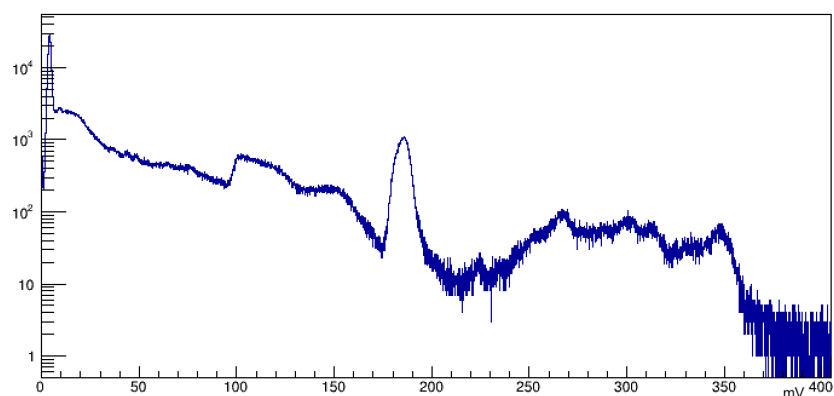
Figure 3.19: Thalia spectrum with IC placed (^{252}Cf source). We observe the intrinsic activity of the detectors as seen previously in Fig. 2.2.

In the ^{252}Cf decay, there is a small percentage (<0.02%) of gamma emission at 43.38,

100.4 and 155.0 keV. In Fig. 3.19, their energies in mV should be around 6, 13 and 20 mV, but they are not statistically relevant in the spectrum.

In Fig. 3.20, we can clearly identify the fissioning sources' gamma emission from the intrinsic activity of the detectors.
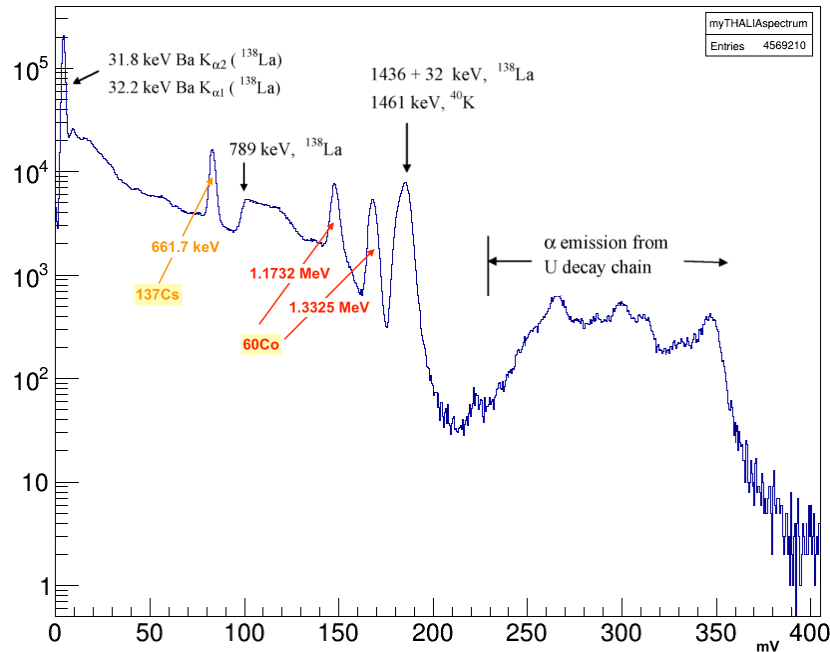
Figure 3.20: Thalia spectrum with ^{60}Co and ^{137}Cs sources.

The fitting parameters of the Co and Cs peaks give the energy intervals that will be used to perform the time coincidence between the detectors and to determine the time resolution of each detector (see Fig. 3.20). From the Gaussian fit plus a polynomial of order one, we obtain, in mV, the average values and the limits of the interval for a confidence interval of 95.45%[5].

- ^{137}Cs (661.7 keV): [79.07, 87.11] mV
- ^{60}Co (1173.2 keV): [142.68, 153.01] mV
- ^{60}Co (1332.5 keV): [163.28, 172.76] mV

3.2.9   Time resolution

The time resolution of a setup of two detectors is determined by the FWHM of the peak formed by subtracting the trigger time of detector 1 and detector 2.

In our setup, the time resolution is determined by the FWHM of the Thalia trigger minus the Cathode time trigger peak (Fig. 3.21). We expected to find a time resolution of around 3 or 4 ns but instead found a resolution of 9 ns, much worse than expected for this fast response detector.

---

[5]The interval estimate in a normal distribution: 68.27% for one σ, 95.45% for $2 \cdot \sigma$ and 99.7% for $3 \cdot \sigma$, where σ is the standard deviation of the mean value.

There are two hypotheses: either we didn't manage to find the proper parameters that improve the time resolution, or there could be some limitation regarding the trace analysis, possibly related to the discretisation of the signal that is later reconstructed in the continuum for the zero crossing measurement.

Figure 3.21: Coincidence peak between Thalia and Cathode trigger time

To evaluate those hypotheses, we perform a time coincidence between the Thalia detector and one of the PARIS detectors with ^{60}Co and ^{137}Cs sources, following the same technique used for Cathode and Thalia. Due to the high intrinsic activity of the detector, we must verify the energy of the gammas detected. We only consider the time coincidence measurements when the gamma energy belongs to one of the energy intervals mentioned in the previous subsection.

As a result, we found a time resolution of the gamma flight between Thalia and one PARIS' phoswhich to be (1.38 ± 0.07) ns. This is a more satisfactory result, but we aim for better precision, which is essential for the time alignment of all detectors of the setup in further analysis (out of the scope of this thesis).

The peak asymmetry is due to the different time resolutions of the detectors; therefore is crucial that the time coincidence never takes the absolute value of the difference between triggers so the asymmetry is kept.

Figure 3.22: Coincidence peak between Thalia and a PARIS phoswhich trigger time

From the resolution of the two detectors (Δ_i and Δ_j) measured from one another, once PARIS time resolution is calculated, we can also calculate the individual resolution of a detector using the following relation [31]:

$$\Delta_{i,j} = \sqrt{\Delta_i^2 + \Delta_j^2} \tag{3.1}$$

3.2.10 Electron drift time

The electron drift time measurement is more complex because it requires different trace alignment and shaping functions. The first step is to align and add the traces. The trigger
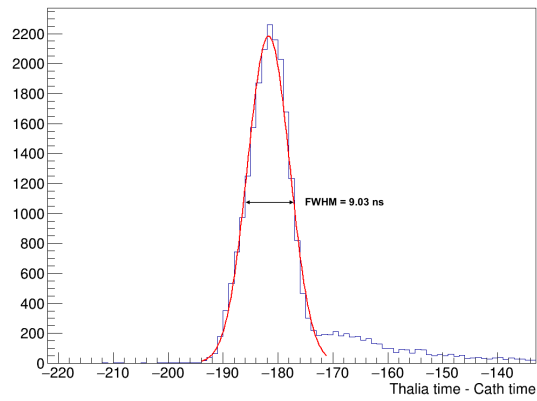
time difference gives the delay between the anode traces (back anode 1 and 2 or front anode 1 and 2). The same applies to the delay between anodes and cathode signals.

The total back or front anode trace is shaped with the following equation[24]:

$$t_n = \frac{1}{Q_{MAX}} \cdot \sum_{k=k_0}^{k_0+n} (s_{k+1} - s_k) \cdot (t_k - t_0) \tag{3.2}$$

Where Q_{MAX} is the total deposited charge; k_0 corresponds to the cathode trigger sample number at t_0 ns; s_k is the sample of number k, which occurs at time t_k. In other words, $(t_k - t_0)$ is the delay between the total back or front anode signal with respect to the cathode signal.

The resulting waveform t_n is now shaped with a CR high-pass filter with a shaping time of 1000 ns to enhance the variations of the signal and completely capture the rising part.

The maximum of the filtered t_n waveform gives the average electron drift time.

By plotting the drift time *versus* the energy spectrum of the anode, we can better visualise the fission fragments' mass separation.
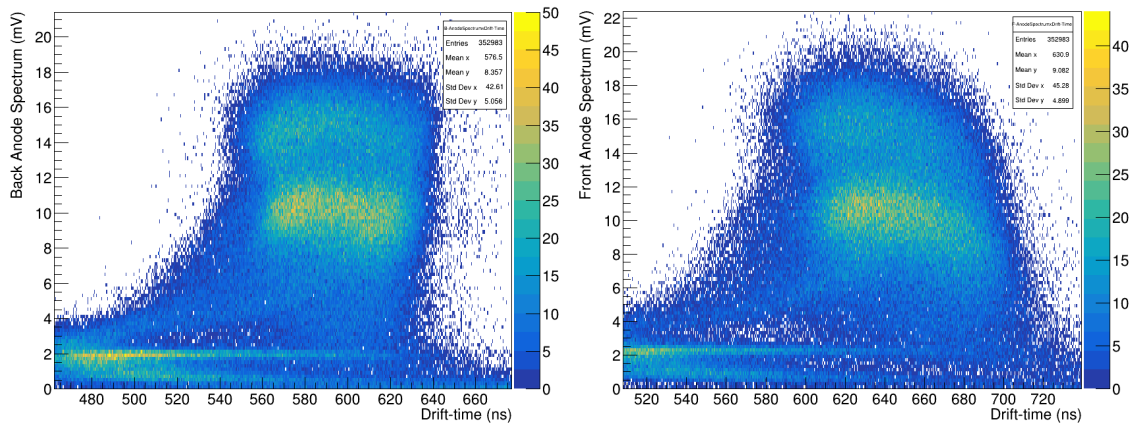
Figure 3.23: Anode spectrum *versus* electron drift time. Back anode (left) and front anode (right).

When the electrons reach the anodes faster, it means that the FF were emitted with smaller angles, so they had shorter routes to travel. In comparison, larger drift times indicate larger angles, which results in longer routes, causing the FF to lose energy. This explains the decay in energy for higher drift times in Fig. 3.23.

3.2.11 Emission angle reconstruction

The angle of emission and the position figures are reconstructed from the equation 2.1, previously presented. The centre of mass of this figure is not centred in zero, indicating that there is a small difference in the output signal scales for different channels, justifying the need to add a scaling factor to align energy measurements obtained from traces coming from different channels.
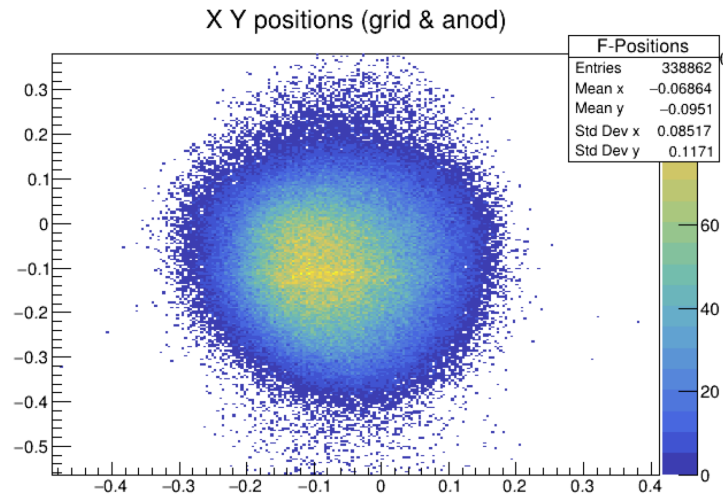
Figure 3.24: Reconstruction of position figure based on equation 2.1.

3.3 Discussion on trace analysis approach

Some difficulties were faced while implementing this analysis technique regarding the correct approach for processing the samples and tuning the best parameters, which is not trivial. While the extensive parameters testing resulted in a good intuition regarding electronics filter simulators in trace analysis, some parts of the analysis were not fully mastered, and some of the results were unsatisfactory, such as the cathode trigger time and the drift time calculation (Fig. 3.23).

Indeed, the drift time strongly depends on the cathode trigger time, which is a plausible justification for the unexpected scattering for lower energies (below the fission fragments region). On the other hand, the cathode trigger is far from ideal, with a time resolution of 9 ns. The CFD is indeed the most reliable trigger time technique for this case since it doesn't depend on the signal amplitude, but its parameters for the cathode signal were not mastered.

When evaluating the crossing zero distribution in a sample, for different CFD fraction values, unwanted discontinuities are formed between sample limits, a consequence of reconstructing the continuous from discrete values of a sample (see Fig. 3.25). Still, that cannot be the cause of poor time resolution since it is only perceptible under 2 ns scale. The number of delayed samples can be smaller since only 3 positive samples are needed, but the number presented in this work was already the one that better improved the resolution. The technique
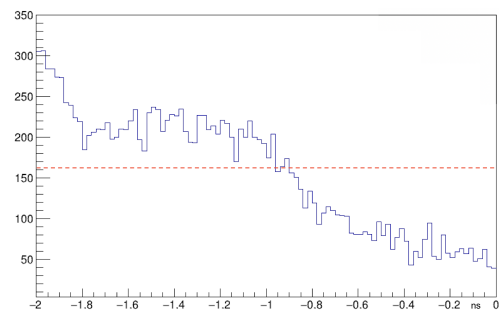
Figure 3.25: Zero crossing position distribution after CFD. The red dashed line indicates the expected distribution behaviour, equal distribution in sample interval (-2,0).

itself is correct as we obtained a proper time resolution for Thalia LaBr$_3$ detector in time coincidence with a PARIS phoswich.

The trace analysis is a very time-consuming technique, not only due to computer processing time consumption but also for pre-analysis and parameter tuning. Unfortunately, this last step remains necessary to build a training set of data for neural network algorithms. This will however not be considered for benchmarking the various methods.

Chapter 4

Neural network model and performance evaluation

The trace analysis method presented is a time-consuming technique; it requires converging to the parameters that give the best time and energy resolution, and once the parameters' values are chosen, each trace is processed at least two times for energy and time measurements.

The characteristic behaviours of cathode, anode and wire plane traces are known, so an NN model can predict the energy and time measurements necessary to reconstruct the fission event through a supervised learning algorithm. To verify the validity of this statement, I started with the simplest approach: each IC component trace has its own neural network model, as it is explained in section 4.2.

4.1 Data sets

The very first step in building a supervised learning NN model is to define the input and output layers necessary for the training, validation and test data sets.

From FASTER raw data files, three inputs must be given to the NN: the trace itself, its respective label and the time stamp. From the Cathode trace alone, our target values are the energy and the trigger time. We do not need the trigger time from the anode traces since it was only used for calculating the drift time. Instead, our target values are the energy and the drift time directly. From the wire plane traces, we only aim for the deposited charge measured from that trace.

This results in a data set with very different data formats; therefore, the data sets are stored in a "TTree". In the ROOT[1] data analysis framework, a "TTree" is a fundamental data structure that stores and organises large amounts of data in a hierarchical format.

---

[1]ROOT is an open-source software framework developed by CERN primarily for use in high-energy physics experiments. More about ROOT features and components can be found in [5].

Drawing a comparison with a standard table, the rows are the entries, and the columns are the "TTree" branches. A scheme of data structure is presented in Fig. 4.1.
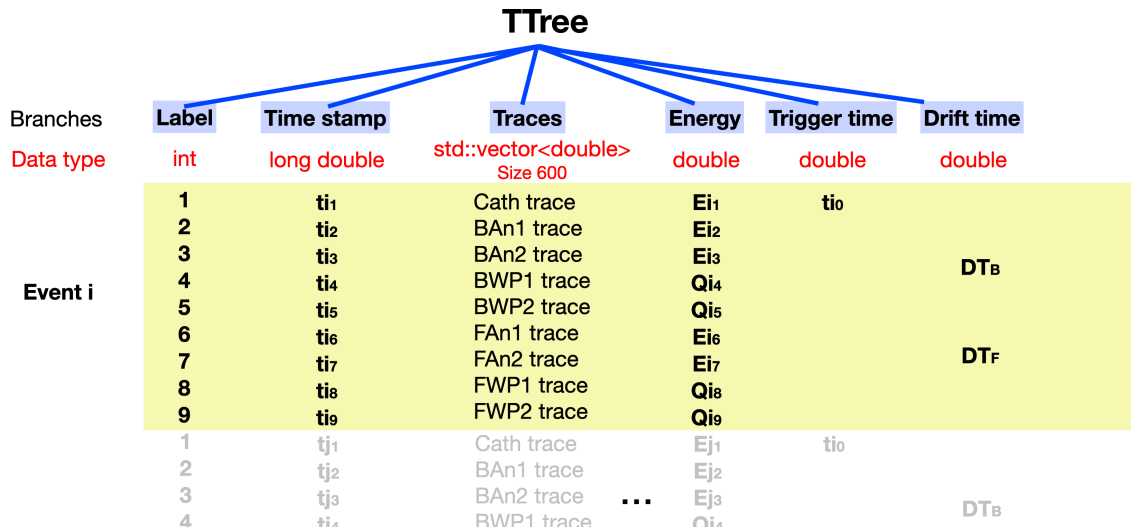

Figure 4.1: Data set format for neural networks. The branches "Label", "Time stamp" and "Traces" are the input data and the "Energy", "Trigger time" and "Drift time" are the target values.

Despite the chosen activation function or neural network model, the data must be normalised so the NN can learn from minimising the loss function. Since our data doesn't have any negative values, the data is normalised to fit the interval (0,1). The normalisation constant C_N of each trace is determined from FASTER acquisition parameters mentioned previously in Table 2.1.

Table 4.1: **Input traces normalisation**

	Cathode	**Anodes and wire planes**
Trace sample amplitude: a.u. to mV	$\frac{2390}{2^{16}}$	$\frac{2390}{2^{19}}$
Maximum amplitude	1200 mV	150 mV
C_N	$30.39 \cdot 10^{-6}$	$243.12 \cdot 10^{-6}$

Table 4.2: **Target values normalisation constants**

	Cathode		**Anodes**		**Wire plane**
Target value	Energy	Trigger time	Energy	Drift time	Deposited charge
C_N	$30.39 \cdot 10^{-6}$	1200^{-1}	$243.12 \cdot 10^{-6}$	1200^{-1}	0.2917

At least three data sets must be created: a training, a validation and a testing data set. It is very important that these three data sets are uncorrelated, so data sets from different experimental runs were used.

The training data set contains information on 113 thousand events, while both other data sets have around 38 thousand, a third of the training data set. Much more data was available, but due to time constraints and computational logistics, the data sets were not increased more than necessary.

4.2 Neural network model

The NN type chosen was a Fully Connected Neural Network (FCNN), where every neuron of one layer is connected to all neurons of the following layer (Fig. 4.2).

The greatest advantage of using an FCNN for trace analysis is their "structure agnostic" behaviour; no assumptions are made from the input. FCNNs are known to be universal function approximators since they can predict continuous functions or target values if the model has enough hidden layers and appropriate activation functions to cap-

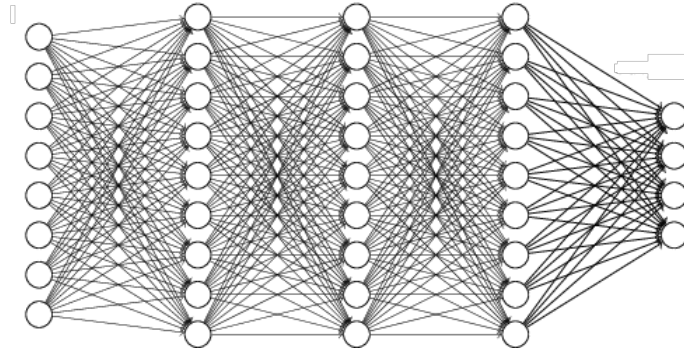Figure 4.2: Fully Connected Neural Network (FCNN). Taken from [29].

ture input data features. Aiming for a regression model, FCNN presents itself as a suitable option due to its flexibility regarding output layer format and type.

If FCNNs are flexible and adaptive for different scenarios, their implementation might not be trivial. There are three major drawbacks. The first one is the necessity of a really large training data set; if one advantage was a large number of parameters to learn data features, small data sets would most certainly be overfitted or at least lead to poor generalisation. The second drawback is the non-triviality of hyperparameter tuning. Selecting the number of layers, the number of neurons per layer and choosing an activation function might require extensive experimentation if there is no intuition about the expected correlation between the input and output layers. Other hyperparameters, such as learning rate and batch size, might also require tuning and experimentation. Finally, if deep architectures are used, the training becomes computationally expensive and time-consuming.

The time-consuming and overfitting disadvantage can be compensated with dropout, which is a regularisation technique that randomly drops neurons during training, being able to identify the most relevant ones for minimising the loss function.

4.2.1 FCNN model design

As mentioned previously, three FCNN models are designed for each IC component (cathode, anode and wire plane).

To build the neural networks, the Keras[13] library was used. Keras is a high-level neural network API[2] written in Python and integrated by TensorFlow[8]. TensorFlow is one of the most popular and widely used open-source machine learning frameworks for building and deploying machine learning and deep learning algorithms.

---

[2]API stands for Application Programming Interface

The following models were built with a Keras sequential model, appropriate for a plain stack of layers where each layer has exactly one input tensor and one output tensor.

Even though the model schemes (e.g. Fig. 4.3) show inputs of shape (nx600), the inputs are concatenated, resulting in an input with shape (1xn·600). As it is a fully connected model, the connections between neurons are valid, and the scheme is only presented as it is for comprehension purposes.

Activation function and loss function

A great advantage of knowing how the target values were calculated is easily predicting which activation function is more suitable for this scenario. The filtering procedures performed in the standard analysis are of first or second order, so the activation function for hidden layers must be ReLU. The Rectified Linear Unit function is linear for positive input values and non-linear for negative values. We can predict second-order correlations with two hidden layers, both activated with ReLU.

For regression models, the loss function can be either Mean Squared Error (MSE) or Mean Absolute Error (MAE). There is also a third hybrid option called Huber Loss, which is the convolution of the absolute value function with the rectangular function, scaled and translated. It behaves as MAE close to zero and MSE for higher errors.

Loss functions such as accuracy or cross-entropy functions are only suitable for binary or classification models.

Optimiser and learning rate

Adam[27] optimisation is a stochastic gradient descent method that is based on adaptive estimation of first-order and second-order moments. It is computationally efficient, doesn't require much memory, and is well-suited for problems that are large in terms of data and/or parameters. This optimiser is also appropriate for problems with noisy and sparse gradients.

The learning rate can be defined with the optimiser. For Adam, the default value for learning rate is 0.001 and it can be tuned by the user.

4.2.2 Cathode traces FCNN model architecture and hyperparameters

This model contains one concatenated input of total size (1x1200), equivalent to (2x600), where the first input is the cathode traces and the second is the time position of each sample [0 ns, 2 ns, 4ns, ..., 1198 ns], normalised with $C_N = 1200^{-1}$.

The hidden layer **1** is common for both outputs and has 600 neurons, the same size as the trace. Then, the NN is split into two hidden layers with 600 neurons each **2a** and **2b**, where **2a** is connected to output **a** and **2b** to output **b**. These steps are very important because the first hidden layer serves to correlate the time and amplitude inputs.

Input layer
Shape 2x600

Hidden layer 1
Shape 1x600

Hidden layer 2a
Shape 1x600

Hidden layer 2b
Shape 1x600

Output layer a
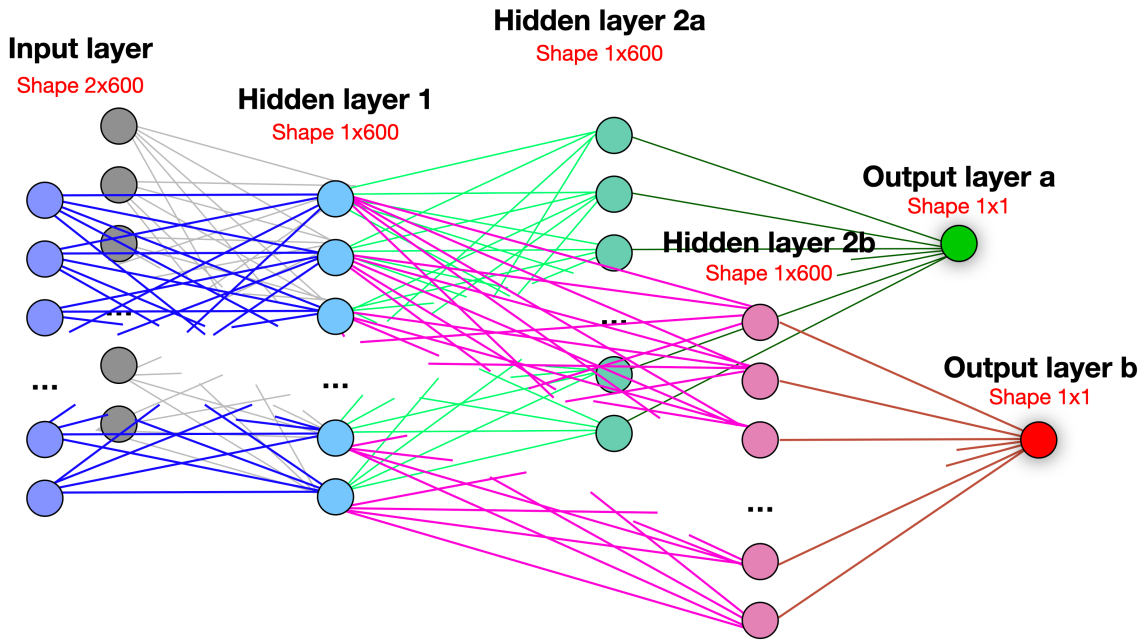Shape 1x1

Output layer b
Shape 1x1

Figure 4.3: Cathode fully connected neural network model for energy and trigger time prediction from traces.

In contrast, the **2a** and **2b** hidden layers serve to recover energy and time features in the data. Hidden layer **2a** has all its neurons connected to the output layer **a** with only one neuron. The exact same happens for the hidden layer **2b** and output layer **b**.

Table 4.3: **Summary of cathode traces FCNN model hyperparameters**

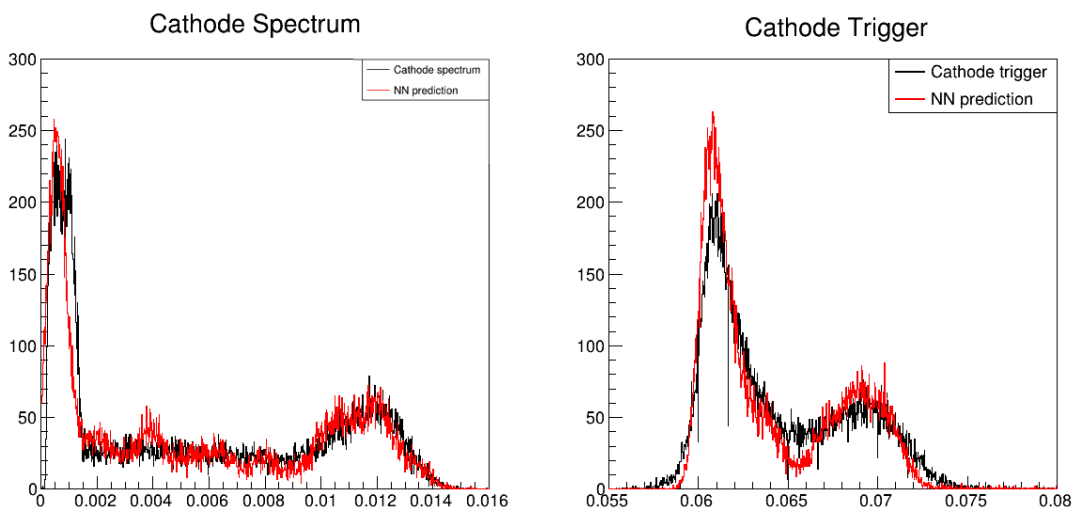| Batch size	Epochs	Learning rate	Number of hidden layers	Optimiser
256	30	0.0001	3	Adam
Activation function:				
Hidden layer 1: ReLU			Hidden layers 2a/b: ReLU	

Cathode Spectrum

Cathode Trigger

Figure 4.4: Cathode FCNN model output predictions compared to usual technique values.

The integral of the second peak in trigger time prediction corresponds to 36% of the to-

tal histogram integral, the same rate previously estimated for the fission fragments. Comparing the trace analysis results and NN prediction trigger time distribution, the separation between FF and non-FF is more prominent for NN. A final conclusion on the efficiency regarding timing resolution can only be made by also performing an NN trace analysis of Thalia for trigger time, later followed by calculating the FWHM of the coincidence peak between both signal times differences. Unfortunately, due to time constraints, this last step couldn't be performed.
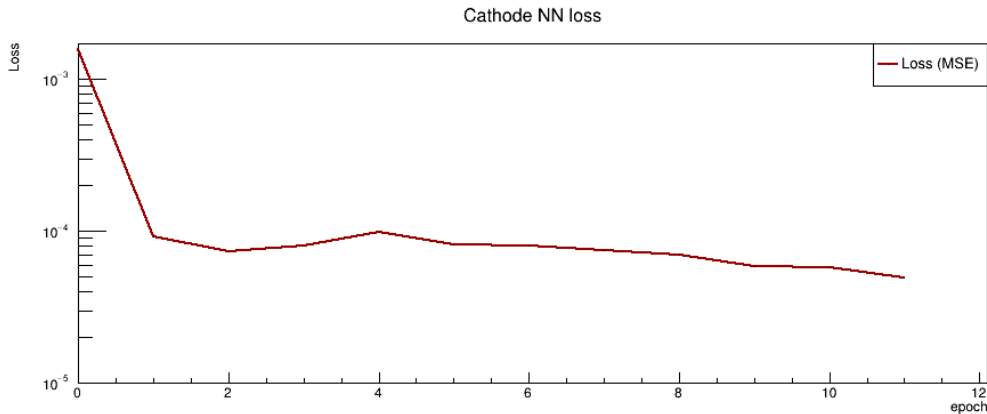

Figure 4.5: Cathode loss

The loss for this model was measured by MSE, and it quickly converged to an optimal solution. This model was evaluated with a loss of $7.24 \cdot 10^{-6}$.

4.2.3 Anode traces FCNN model architecture and hyperparameters

Model 1: Hidden layer 1 common to energy and drift time output

The first model built for the anode's traces contains one concatenated input of total size (1x1800), equivalent to (3x600), where the two inputs are the back or front anode 1 and 2 traces. The third is the time position of each sample [0 ns, 2 ns, 4ns, ..., 1198 ns], normalised with $C_N = 1200^{-1}$, corresponding to the x-axis of the trace. Unlike in the cathode model, the anode energy and drift time are measured from the total back or front anode signal, so both traces must be given as inputs. There is no need to give the x-axis twice since they are the same.

The hidden layer **1** is common for two outputs and has 600 neurons. Then, the NN is split into two hidden layers with 600 neurons each **2a** and **2b**, where **2a** is connected to output **a** and **2b** to output **b**, for the same reasons as the previous model. Hidden layer **2a** has all its neurons connected to the output layer **a** with only one neuron. The exact same happens for the hidden layer **2b** and output layer **b**.

The batch size in the anode traces prediction model is 4 times higher than the cathode model because the anode input is more complex, and we want to avoid overfitting.

Unfortunately, despite the extensive hyperparameter tuning, the model failed to predict
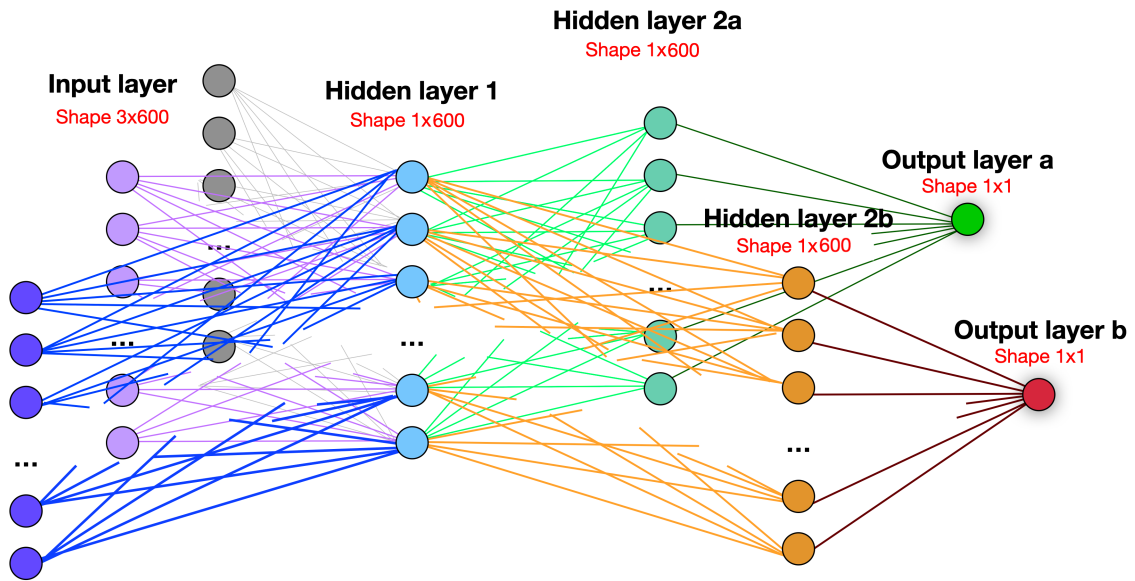
Figure 4.6: Anodes fully connected neural network model for energy and drift time prediction from traces.

Table 4.4: **Summary of anode traces FCNN model 1 hyperparameters**

Batch size	Epochs	Learning rate	Number of hidden layers	Optimiser
1024	30	0.0001	3	Adam
Activation function:				
Hidden layer 1: ReLU			Hidden layers 2a/b: ReLU	
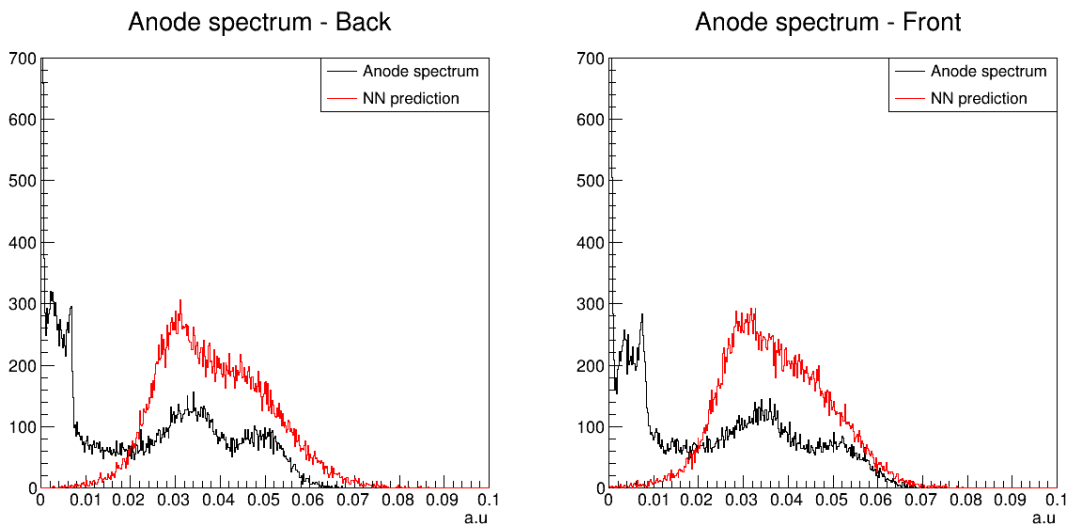
Figure 4.7: Back anode spectrum (left) and Front anode spectrum (right). The black histograms correspond to the energy values obtained from the trace analysis technique, and the red histograms are the predictions made by the NN model. The x-axis has arbitrary units.

the anode spectrum with the same resolution. The better the energy resolution, the better one can distinguish the two spectrum peaks corresponding to the FF.

As expected, the drift time prediction proved to be more challenging and influenced the energy prediction. While the filters applied to a trace have a linear behaviour, the

Figure 4.8: Trace analysis and NN predicted drift time distributions. The x-axis has arbitrary units, and peaks are centred in arbitrary values for better visualisation.
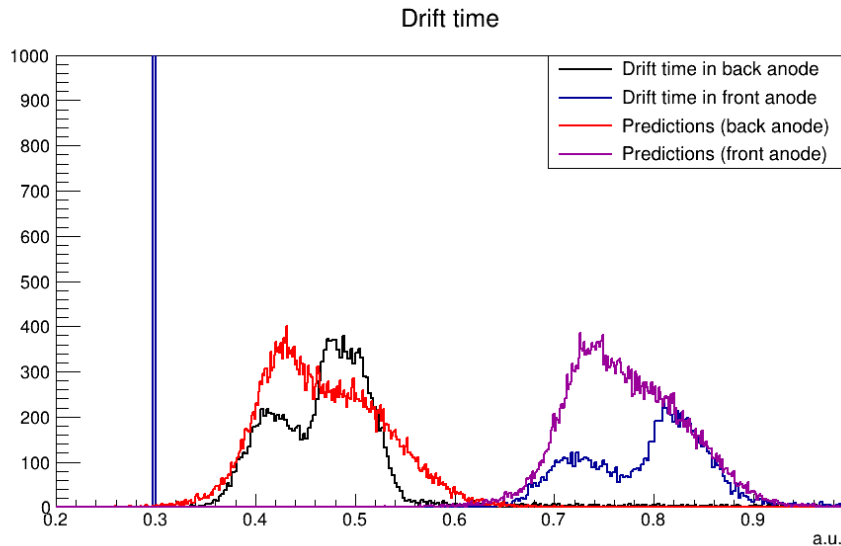
same doesn't apply to the shaping performed for the drift time calculation. The drift time also depends on the cathode time trigger, so the drift time value used for training was corrected based on the difference between the anodes' time stamps and the cathode's in the hope that the neural network could recognise the drift time in the time window of the anodes traces.

To improve the energy resolution for the anode spectrum, another model was built to process the energies and drift time separately.

Figure 4.9: Anode loss in model 1
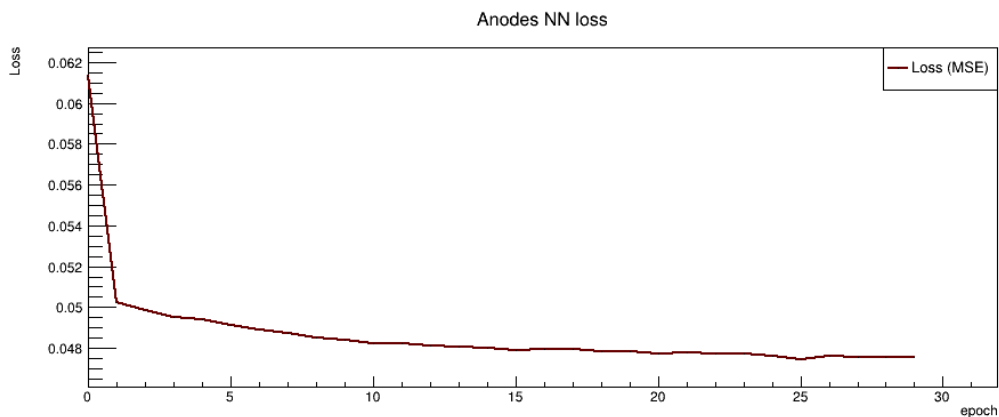
This model was evaluated with a loss of 0.0496.

Model 2 and 3: independent energy and drift time prediction

The second model built for the anode's traces contains one concatenated input of total size (1x1200), equivalent to (2x600), where the two inputs are the back or front anode 1 and 2 traces. It has two hidden layers, **1** and **2**, with 1200 neurons each connected to the

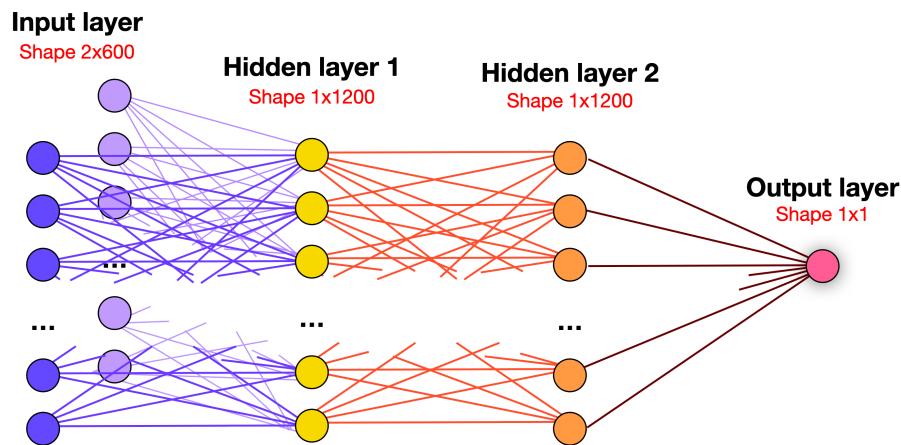single output that targets the energy value (see Fig. 4.10).

Figure 4.10: Anodes fully connected neural network model for energy prediction from traces.

The third model built for the anode's traces contains one concatenated input of total size (1x1800), equivalent to (3x600), where the first two inputs are the back or front anode 1 and 2 traces, and the third is the normalised time position of each sample. It has two hidden layers, **1** and **2**, with 1200 neurons each connected to the single output that targets the drift time value (see Fig. 4.11).
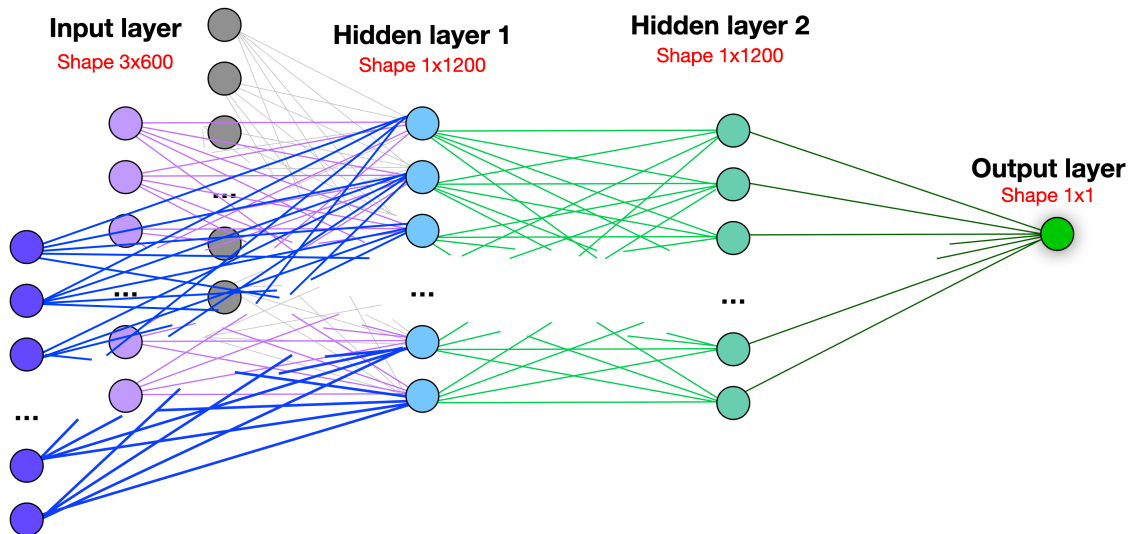
Figure 4.11: Anodes fully connected neural network model for drift time prediction from traces.

Table 4.5: **Summary of anode traces FCNN model 2 and 3 hyperparameters**

Both models have the following hyperparameters:

Batch size	Epochs	Learning rate	Number of hidden layers	Optimiser
256	30	0.0001	3	Adam
Activation function:				
Hidden layer 1: ReLU			Hidden layer 2: ReLU	

Model 2 successfully predicted the anode spectrum without deteriorating the energy

resolution.

Figure 4.12: Anode FCNN model 2 output spectrum predictions compared to results of usual trace analysis. The back anode corresponds to the left and the front anode to the right graph.
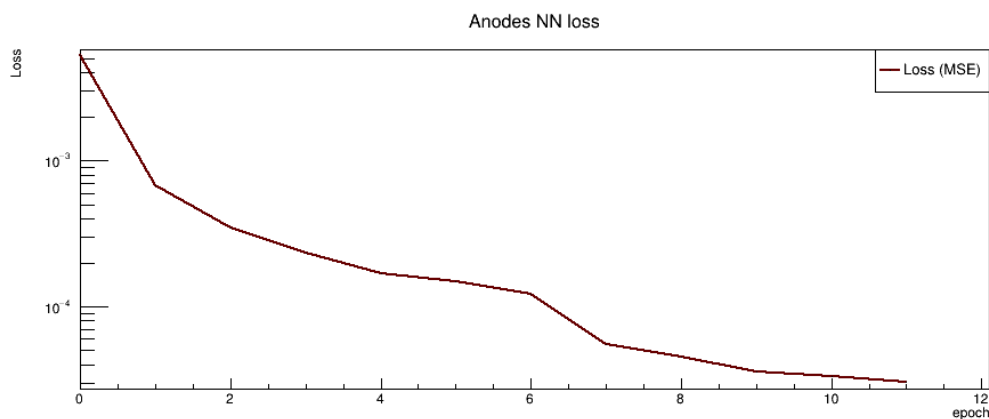
Figure 4.13: Anode FCNN model 2 output spectrum loss (mean absolute error).

Due to normalisation, the values for the anode spectrum were very close to zero (below 0.001). To improve the performance of the NN, the loss function was set to Mean Absolute Error (MAE) instead of Mean Squared Error (MSE) applied in the other models. Anode model 2 was evaluated with a loss of $2.64 \cdot 10^{-5}$.
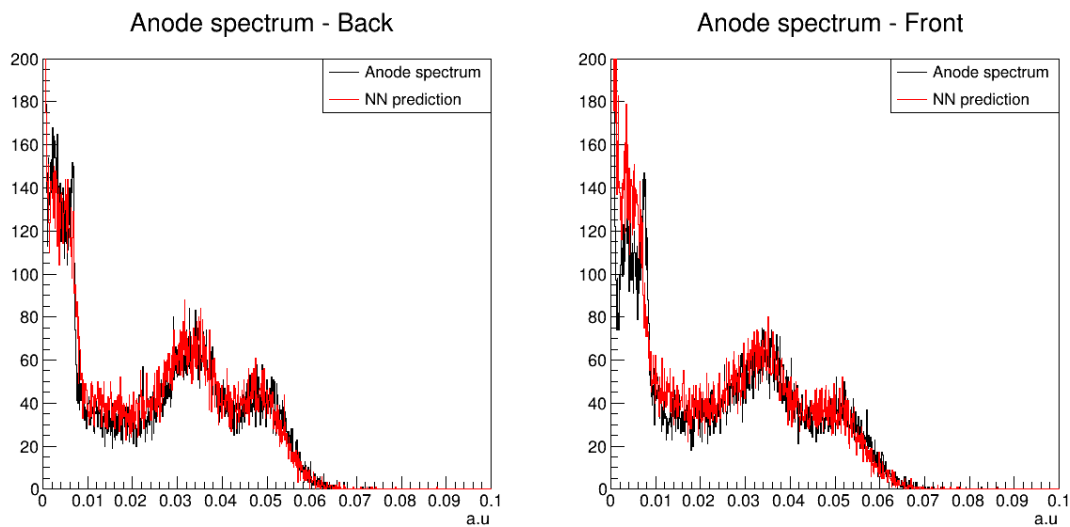
Model 3 predicted the drift time better for the back anode but still failed for the front anode. In the various models tested, the loss function was never below 0.048, showing that the NN structure cannot predict the drift time value only from the anode traces.

Anode model 3 was evaluated with a loss of 0.0488. In further analysis, the usual trace analysis methods parameters must be verified to ensure the training values are correct and different architectures must be tested.

Another way of evaluating model 2 and 3 quality is to plot a similar image to Fig. 3.23 with the NN predictions (see Fig. 4.16).
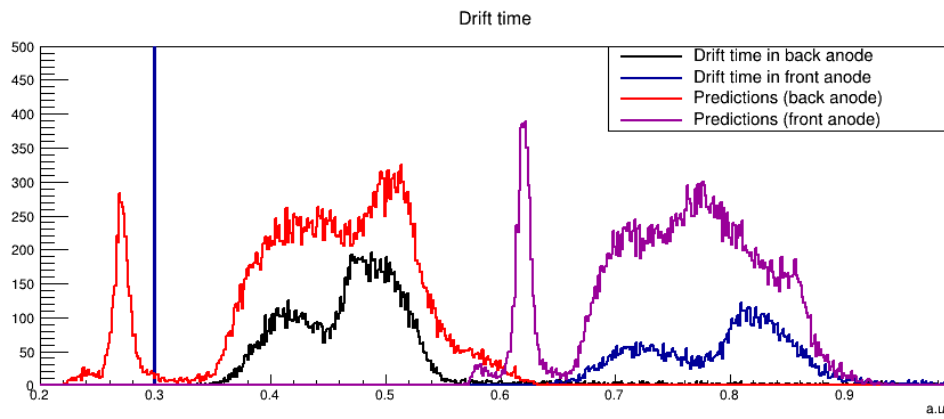
Figure 4.14: Anode FCNN model 3 output drift time predictions compared to results of usual trace analysis methods.
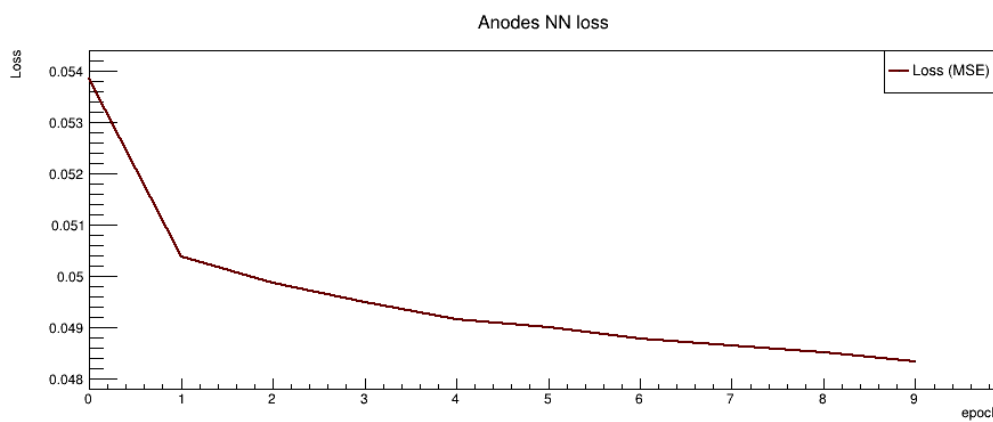
Figure 4.15: Anode FCNN model 3 output drift time loss (mean squared error).
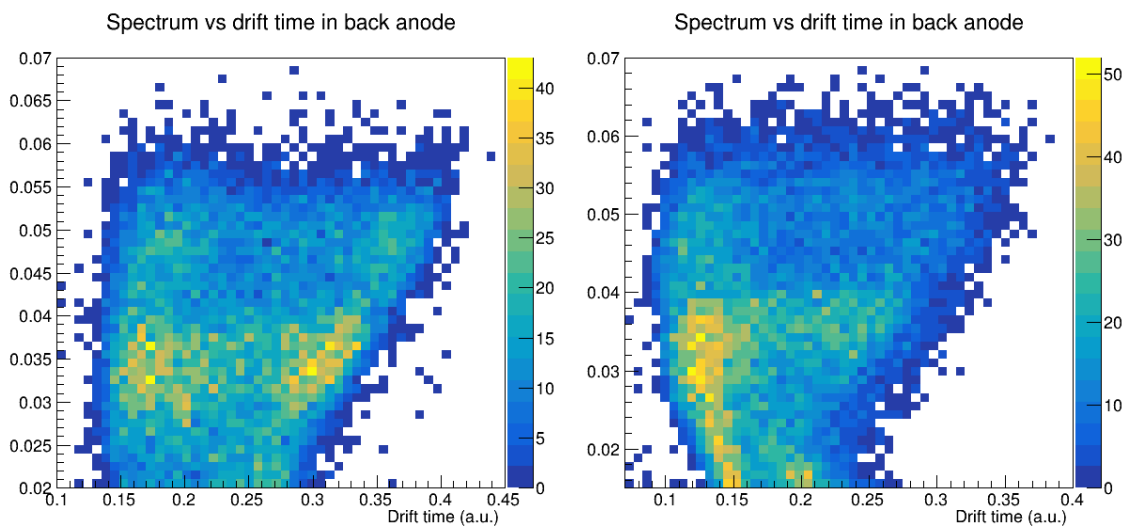
Figure 4.16: Predicted spectrum in y-axis and predicted drift time in x-axis.

The figures are zoomed on the FF regions (from integral statistics), and no meaningful structure can be identified. Indeed, there are fewer statistics than in Fig. 3.23, but with a correct prediction of drift time, a figure with a similar shape is expected.

4.2.4   Wire plane traces FCNN model architecture and hyperparameters

This model contains one concatenated input of total size (1x1200), equivalent to (2x600), where the first input is the trace of a wire plane (back WP 1, back WP 2, front WP 1 or front WP 2). The second is the time position of each sample [0 ns, 2 ns, 4ns, ..., 1198 ns], normalised with $C_N = 1200^{-1}$, corresponding to the x-axis of the trace.
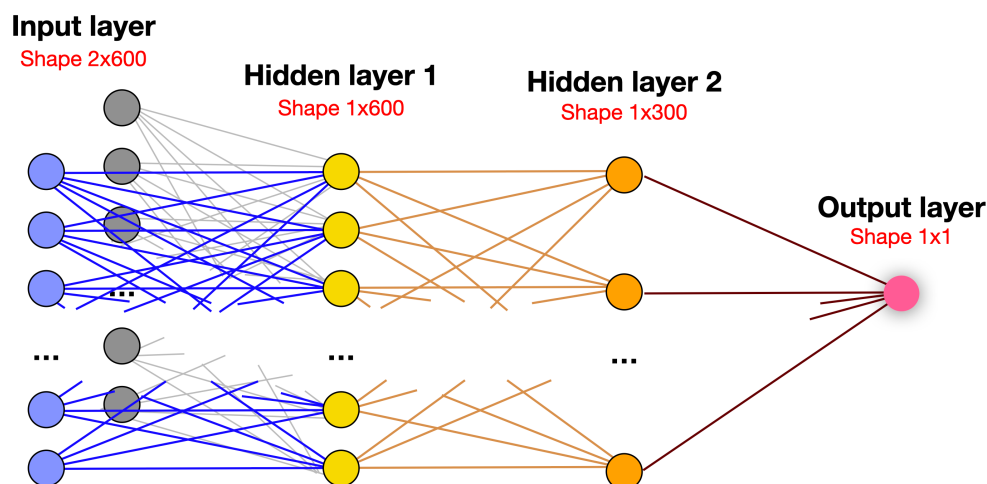
Figure 4.17: Wire plane fully connected neural network model for deposited charge prediction from traces.

The hidden layer **1** has 600 neurons, the same size as one trace. The second hidden layer **2** has 300 neurons and is connected to the only output layer with one neuron. The number of neurons in hidden layer **2** is half of the first to better generalise the features of a wire plane trace. This approach is better than giving the four traces at once and receiving the four deposited charges predictions because it reduces the computational cost and improves the loss function.

Table 4.6: **Summary of wire plane traces FCNN model hyperparameters**

Batch size	Epochs	Learning rate	Number of hidden layers	Optimiser
256	30	0.0001	2	Adam
Activation function:				
Hidden layer 1: ReLU			Hidden layer 2: ReLU	

The wire plane charge deposited the prediction model was very successful for all wire plane traces, proving that this neural network is robust to traces obtained from different channels with scaling variations, only requiring post-calibration.

This model was evaluated with a loss of $1.01 \cdot 10^{-7}$.
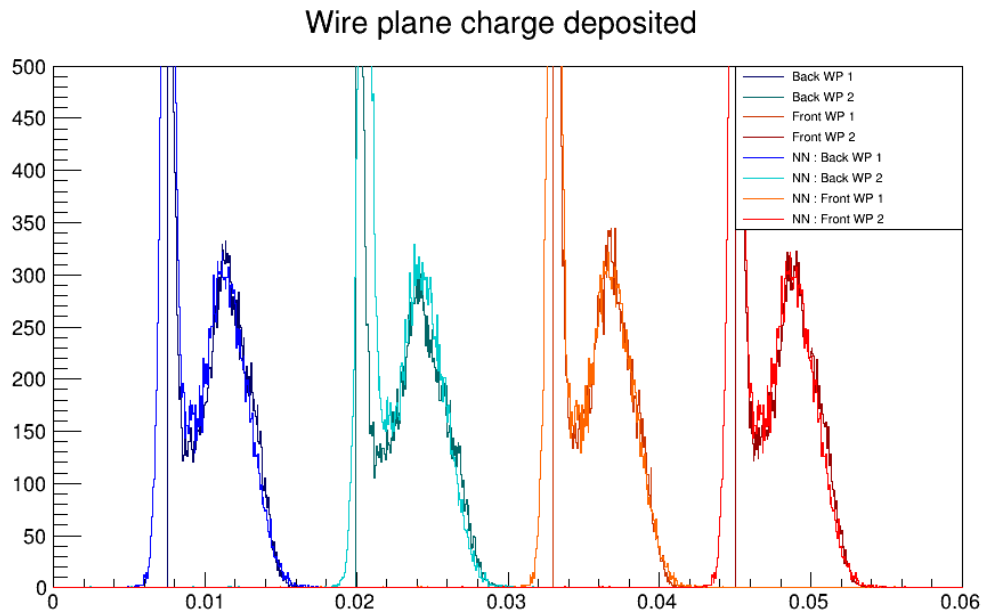
Figure 4.18: Wire plane deposited charges and their respective NN predictions.
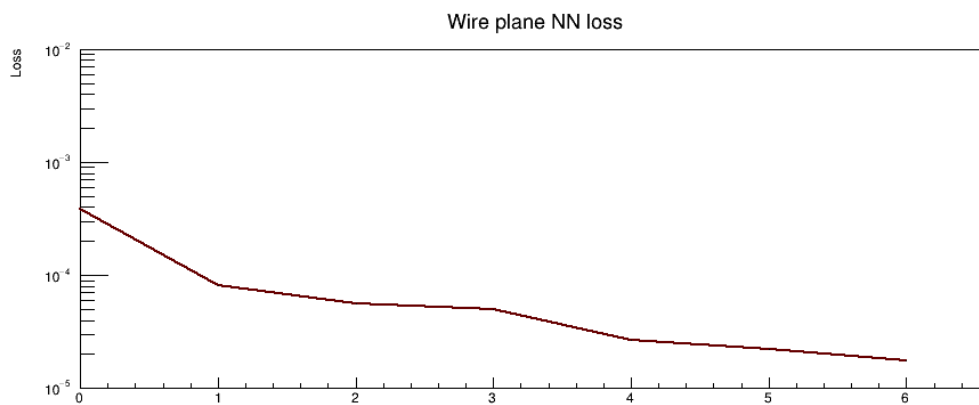
Figure 4.19: Wire plane NN model loss.

4.3 Performance of FCNN models and comparison with standard analysis

At this point, two trace analysis techniques have been presented in detail, and a qualitative and quantitative evaluation must be made.

Regarding the implementation of neural networks *versus* the conventional approach, we also aim to answer the following:

- Do we gain time in the analysis by using artificial intelligence?
- Is the computational cost lower than the usual trace analysis technique?
- Does the NN prediction degrade or improve the time and energy resolutions?
- What are the perspectives regarding trace analysis via neural networks?

To evaluate the performance of the neural network approach, we should look at the

computing time involving this method and compare it to the commonly used trace analysis technique.

Table 4.7: **Fully connected NN models total computing time**

Total data size (# traces)	Converting data format		Normalisation
$1.7 \cdot 10^6$	2 m 50.6 s		12.0 s
	Training	**Validation**	**Prediction**
Data size (# traces)	$1.1 \cdot 10^5$	$4 \cdot 10^4$	$4 \cdot 10^4$
Cathode model	1 m 06.3 s	4.7 s	6.8 s
Data size (# traces)	$4.4 \cdot 10^5$	$1.5 \cdot 10^5$	$1.5 \cdot 10^5$
Anode model 1	6 m 44.2s	17.2 s	24.9 s
Anode model 2	3 m 56.9 s	19.0 s	17.6 s
Anode model 3	5 m 44.4 s	26.0 s	15.2 s
Wire plane model	1 m 42.6 s	13.4 s	28.5 s

Once a neural network is trained and validated, the computational consumption is only the data conversion, normalisation and NN prediction. To reconstruct 10^6 events ($9 \cdot 10^6$ traces), using the NN models developed (cathode, wire plane and anode models 2 and 3) would require 1498.6 s, being 1397.3 s for prediction only. In contrast, the trace analysis method takes $14.5 \cdot 10^3$ s or 4h to obtain the same parameters in an equivalent format for a million events (9 million traces). The NN presents a time improvement of over 7.6 times. From the half a billion events, only 36% are expected to correspond to fission fragments data.

During data acquisition, on average, one file is stored every 10 s with 1 Gb of data and has 7700 events, so we can estimate the total computing time each technique requires. With the FASTER acquisition parameters referenced in this work, there are at least 73 thousand files to be analysed, totalling 8.5 days of continuous acquisition time or half a billion events. The usual trace analysis is estimated to take 3 months to process (considering all the tuning was previously done). By altering the data storage format for a more efficient way of accessing the memory, this value can be optimised. Still, it will always require several days because the trace analysis alone, without data storage, is estimated to take 74 days. With NN implementation, it is expected to take 12 days, already considering the data conversion and normalisation computing time, an improvement of at least 6.2 times. However, the preliminary results are very promising, indicating the potential of NN implementation in trace analysis.

As it is today, the neural network models cannot replace the trace analysis for drift time calculation because a suitable architecture was not found due to time constraints.

However, if the drift time is unnecessary, the algorithm can be implemented immediately. The time comparisons without drift time are 19 days for usual trace analysis and 10 days for NN prediction, reducing the processing time by almost half.

Conclusion

In the scope of the Fission Reaction at Orsay with Zero Emission of Neutron (FRØZEN) project, a 5-week experiment labelled "N-SI-125" was held at the ALTO facility in Orsay to investigate the correlations between individual fission fragment pairs and fission observables to describe the entire fission fragment de-excitation process [3]. The ν-Ball2 setup was complemented with a double Frisch-Grid Ionisation Chamber (IC) that serves a few purposes. It is the fission tag of the experiment is used to calculate the time resolution and perform the time alignment between detectors. It allows the determination of the fission fragments (FF) kinematic properties, such as energy and the emission angle. Some properties of IC traces justify the data acquisition as sampler or traces; hence, the trace analysis aims for better time resolution and calculations such as the electron drift-time, which cannot be done by FASTER data acquisition. The trace analysis is a computationally expensive, time-consuming technique, so there is a great interest in developing neural networks for faster and more efficient trace analysis. For instance, from the six months of my work at IJCLab, 5 weeks were dedicated to the experiment, and at least four months were solemnly dedicated to the usual trace analysis approach: parameter identification, code (re)writing and debugging, leaving less than a month for NN development.

This work started with detailed information on the experimental setup of the N-SI-125 experiment and the challenges faced during the campaign as the solutions found for each problem. This is an important step for comprehending the type of data acquired and to be analysed.

The second part of this work consists of performing the trace analysis of the 9 ionisation chamber components' traces, an extensive and time-consuming technique. Many parameters for each IC channel must be tuned to improve time and energy resolutions. While the IC cathode is more relevant for timing, the 4 wire plane and 4 anode channels give important energy information and allow the reconstruction of the fission fragments' emission angle. Once the best parameters are found and all data can be analysed, the computing time is still a major drawback. While the energy calculation was successfully mastered, the trigger time presented to be much more challenging. If a time resolution of less than 1 ns was expected, from the best parameters, a time resolution of 9 ns was found. Unfortunately, it most certainly affects the drift-time calculation as well. The spectra, time coincidence, drift time and angle reconstruction figures, and computing time

statistics are presented.

The third part of this work focuses on developing Fully Connected Neural Networks to predict the trace analysis results solemnly based on the raw traces. The energy values prediction was very successful, and due to time constraints, the evaluation of time resolution for this approach could not be finalised. The figures for trigger time distribution indicate a successful prediction. The drift time, on the other hand, could not be well predicted with the neural network models designed. Due to time constraints, other approaches, such as recursive or convolutional neural networks, couldn't be tested.

Despite the challenges of this exploratory work, promising results were found as the time consumption of the neural networks prediction of the IC trace features is considerably smaller than the usual trace analysis technique. To process all the data acquired during the experiment, the usual analysis approach would take 74 days, while the neural networks would take 12 days, an improvement of 6.2 times.

References

[1] A. Al-Adili, V. Rakopoulos, and A. Solders, Eur. Phys. J. A 55 (2019), 61.

[2] L. Qi et al., Phys. Rev. C 98 (2018), 014612. and L. Qi et al., Eur. Phys. J. A 56 (2020), 98.

[3] HDR Université Paris-Saclay: The γ emission in the fission process. Matthieu Lebois. 2021.

[4] PARIS - a project for a novel scintillator array based on LaBr3. Presented by Adam Maj IFJ PAN Krakow. http://paris.ifj.edu.pl/file/Maj_PARIS_RISP2012.pdf.

[5] Rene Brun and Fons Rademakers, ROOT - An Object Oriented Data Analysis Framework, Proceedings AIHENP'96 Workshop, Lausanne, Sep. 1996, Nucl. Inst. Meth. in Phys. Res. A 389 (1997) 81-86.

[6] *FASTER SAMPLER MnM USER MANUAL*. Accessed on 2023-09-13.

[7] Alto - accélérateur linéaire et tandem à orsay, Jul, 2023. https://alto2dot0.sciencesconf.org/resource/page/id/2.html.

[8] M. Abadi, A. Agarwal, P. Barham, E. Brevdo, Z. Chen, C. Citro, G. S. Corrado, A. Davis, J. Dean, M. Devin, S. Ghemawat, I. Goodfellow, A. Harp, G. Irving, M. Isard, Y. Jia, R. Jozefowicz, L. Kaiser, M. Kudlur, J. Levenberg, D. Mané, R. Monga, S. Moore, D. Murray, C. Olah, M. Schuster, J. Shlens, B. Steiner, I. Sutskever, K. Talwar, P. Tucker, V. Vanhoucke, V. Vasudevan, F. Viégas, O. Vinyals, P. Warden, M. Wattenberg, M. Wicke, Y. Yu, and X. Zheng. TensorFlow: Large-scale machine learning on heterogeneous systems, 2015. Software available from tensorflow.org.

[9] R. Abbott, T. D. Abbott, S. Abraham, and et al. Prospects for observing and localizing gravitational-wave transients with advanced ligo, advanced virgo and kagra. *Physical Review D*, 101:055001, 2020.

[10] D. Alexiev, L. Mo, D. Prokopovich, M. Smith, and M. Matuchova. Comparison of and with nai(tl) and cadmium zinc telluride (czt) detectors. *Nuclear Science, IEEE Transactions on*, 55:1174 – 1177, 07 2008.

[11] M. Bender, R. Bernard, G. Bertsch, S. Chiba, J. Dobaczewski, N. Dubray, S. A. Giuliani, K. Hagino, D. Lacroix, Z. Li, P. Magierski, J. Maruhn, W. Nazarewicz,

J. Pei, S. Péru, N. Pillet, J. Randrup, D. Regnier, P.-G. Reinhard, L. M. Robledo, W. Ryssens, J. Sadhukhan, G. Scamps, N. Schunck, C. Simenel, J. Skalski, I. Stetcu, P. Stevenson, S. Umar, M. Verriere, D. Vretenar, M. Warda, and S. Åberg. Future of nuclear fission theory. *Journal of Physics G: Nuclear and Particle Physics*, 47(11):113002, oct 2020.

[12] J. Brownlee. Dimensionality reduction for machine learning, Jul, 2023.

[13] F. Chollet et al. Keras. https://keras.io, 2015.

[14] W. contributors. Caesium-137 decay scheme, Jul, 2023.

[15] W. contributors. Cobalt-60 decay scheme, Jul, 2023.

[16] E. Doucet, T. Brown, P. Chowdhury, C. Lister, C. Morse, P. Bender, and A. Rogers. Machine learning n/γ discrimination in clyc scintillators. *Nuclear Instruments and Methods in Physics Research Section A: Accelerators, Spectrometers, Detectors and Associated Equipment*, 954:161201, 2020. Symposium on Radiation Measurements and Applications XVII.

[17] X. Fabian, G. Baulieu, L. Ducroux, O. Stézowski, A. Boujrad, E. Clément, S. Coudert, G. de France, N. Erduran, S. Ertürk, V. González, G. Jaworski, J. Nyberg, D. Ralet, E. Sanchis, and R. Wadsworth. Artificial neural networks for neutron/γ discrimination in the neutron detectors of neda. *Nuclear Instruments and Methods in Physics Research Section A: Accelerators, Spectrometers, Detectors and Associated Equipment*, 986:164750, 2021.

[18] L. Foreman, P. Kleban, L. D. Schmidt, and H. T. Davis. Drift velocities of electrons in methane-inert-gas mixtures. *Phys. Rev. A*, 23:1553–1557, Mar 1981.

[19] C. Fu, A. Di Fulvio, S. Clarke, D. Wentzloff, S. Pozzi, and H. Kim. Artificial neural network algorithms for pulse shape discrimination and recovery of piled-up pulses in organic scintillators. *Annals of Nuclear Energy*, 120:410–421, 10 2018.

[20] N. D. Group. Nuclear data for cf-252 decay probabilities, Jul, 2023.

[21] N. D. Group. Nuclear data for co-60 decay probabilities, Jul, 2023.

[22] N. D. Group. Nuclear data for cs-137, Jul, 2023.

[23] A. Göök, M. Chernykh, J. Enders, A. Oberstedt, and S. Oberstedt. Particle emission angle determination in frisch grid ionization chambers by electron drift-time measurements. *Nuclear Instruments and Methods in Physics Research Section A: Accelerators, Spectrometers, Detectors and Associated Equipment*, 621(1):401–405, 2010.

[24] A. Göök, W. Geerts, F.-J. Hambsch, S. Oberstedt, M. Vidali, and S. Zeynalov. A position-sensitive twin ionization chamber for fission fragment and prompt neutron correlation experiments. *Nuclear Instruments and Methods in Physics Research Section A: Accelerators, Spectrometers, Detectors and Associated Equipment*, 830:366–374, 2016.

[25] Z. He. Review of the shockley–ramo theorem and its application in semiconductor gamma-ray detectors. *Nuclear Instruments and Methods in Physics Research Section A: Accelerators, Spectrometers, Detectors and Associated Equipment*, 463(1):250–267, 2001.

[26] S. Jain. Fundamentals of deep learning - regularization techniques, Jul 2023.

[27] D. P. Kingma and J. Ba. *arXiv*, 2014.

[28] M. Lebois, N. Jovančević, D. Thisse, R. Canavan, D. Étasse, M. Rudigier, and J. Wilson. The v-ball γ-spectrometer. *Nuclear Instruments and Methods in Physics Research Section A: Accelerators, Spectrometers, Detectors and Associated Equipment*, 960:163580, 2020.

[29] "mathandy" (profile: https://math.stackexchange.com/users/53784/mathandy). A name for layered directed graph as in a fully-connected neural network. Mathematics Stack Exchange. URL:https://math.stackexchange.com/q/2048722 (version: 2017-01-19).

[30] A. Said and F. Sayed Ibrahim. Comparative study of segmentation techniques for detection of tumors based on mri brain images. *International Journal of Biochemistry and Biotechnology*, 8:10, 09 2017.

[31] P.-A. Söderström, E. Açıksöz, D. Balabanski, F. Camera, L. Capponi, G. Ciocan, M. Cuciuc, D. Filipescu, I. Gheorghe, T. Glodariu, J. Kaur, M. Krzysiek, C. Matei, T. Roman, A. Rotaru, A. Şerban, A. State, H. Utsunomiya, and V. Vasilca. Eligant-gn — eli gamma above neutron threshold: The gamma-neutron setup. *Nuclear Instruments and Methods in Physics Research Section A: Accelerators, Spectrometers, Detectors and Associated Equipment*, 1027:166171, 2022.

[32] J. Wilson, D. Thisse, M. Lebois, and et al. Angular momentum generation in nuclear fission. *Nature*, 590(7847):566–570, 2021.